

# The Role of Air-Sea Interaction in Controlling the Optimal Perturbations of Low-Frequency Tropical Coupled Ocean-Atmosphere Modes

A. M. Moore<sup>1</sup>, J. Vialard<sup>2</sup>,  
A. T. Weaver<sup>3</sup>, D. L. T. Anderson,  
R. Kleeman<sup>4</sup> and J. R. Johnson<sup>1</sup>

Research Department

<sup>1</sup>Program of Atmospheric and Oceanic Sciences, University of Colorado, Boulder, U.S.A.

<sup>2</sup>LODYC, Universite Pierre et Marie Curie, Paris, France

<sup>3</sup>Centre Européen de Recherche et de Formation Avancée en Calcul Scientifique, Toulouse, France

<sup>4</sup>Courant Institute for Mathematical Sciences, New York University, New York, U.S.A.

Dec. 2001

*This paper has not been published and should be regarded as an Internal Report from ECMWF.*

*Permission to quote from it should be obtained from the ECMWF.*



European Centre for Medium-Range Weather Forecasts  
Europäisches Zentrum für mittelfristige Wettervorhersage  
Centre européen pour les prévisions météorologiques à moyen terme

For additional copies please contact

The Library  
ECMWF  
Shinfield Park  
Reading  
RG2 9AX  
library@ecmwf.int

Series: ECMWF Technical Memoranda

A full list of ECMWF Publications can be found on our web site under:

<http://www.ecmwf.int/pressroom/publications/>

©Copyright 2002

European Centre for Medium Range Weather Forecasts  
Shinfield Park, Reading, RG2 9AX, England

Literary and scientific copyrights belong to ECMWF and are reserved in all countries. This publication is not to be reprinted or translated in whole or in part without the written permission of the Director. Appropriate non-commercial use will normally be granted under the condition that reference is made to ECMWF.

The information within this publication is given in good faith and considered to be true, but ECMWF accepts no liability for error, omission and for loss or damage arising from its use.

## Abstract

In this paper we explore the structure and dynamics of the optimal perturbations of low-frequency coupled ocean-atmosphere oscillations using a hierarchy of hybrid coupled models. Each model is configured for the tropical Pacific ocean and shares a common ocean general circulation model. Three different atmospheric models are used: a statistical model, a dynamical model, and a combination of a dynamical model and boundary layer model. Each coupled model possesses a coupled ocean-atmosphere eigenmode oscillation with a period of the order of several years. The properties of these various eigenmodes and their corresponding adjoint eigenmodes are explored.

The optimal perturbations of each coupled model for two different perturbation growth norms are also examined, and their behaviour can be understood in terms of the properties of the aforementioned eigenmode oscillations. It is found that the optimal perturbation spectrum of each coupled model is dominated by one member. This dominant optimal perturbation evolves into the most unstable eigenmode of the system. The structure of the optimal perturbations of each model is found to be controlled by the dynamics of the atmospheric model and air-sea interaction processes. For the coupled model with a statistical atmosphere, the optimal perturbation center of action is spread across the entire tropical Pacific in the form of a dipole. For the coupled models that include deep atmospheric convection, the optimal perturbation center of action is primarily confined to the western Pacific warm pool. In addition, the degree of linear dependence of the eigenmodes on the remaining members of the eigenmode spectrum is controlled by the atmospheric model dynamics. These findings are in general agreement with the results obtained from intermediate coupled models. In particular, the atmospheric models used here have also been used in intermediate coupled models that have been employed extensively in previous studies of the optimal perturbations of El Niño Southern Oscillation. Thus a direct comparison between those intermediate models and the hybrid models used here can be made.

## 1 Introduction

The need to improve probabilistic forecasts of ENSO has led to a flurry of interest in the optimal perturbations and optimal forcing patterns of the coupled ocean-atmosphere system. The optimal perturbations of a variety of coupled models of ENSO of varying complexity have been discussed in the literature, although there is considerable disagreement between them for a given perturbation growth norm. Some models suggest a pronounced ENSO-like response resulting from perturbations in the eastern tropical Pacific (Blumenthal, 1991; Xue *et al.*, 1994, 1997ab; Chen *et al.*, 1997; Thompson 1998; Fan *et al.*, 2000), while other models yield the same response resulting from perturbations in the west Pacific (Moore and Kleeman, 1996, 1997ab; Eckert, 1999). The latter support the popular idea that intraseasonal variability in the tropical atmosphere may act to enhance or even trigger ENSO episodes (Lau and Chan, 1985, 1986, 1988; McPhaden, 1999). However, the optimal perturbation structure can depend critically on the physics employed in a model and on the number of model degrees of freedom (Moore and Kleeman, 2001).

Most previous studies of optimal perturbations have focussed on models of intermediate complexity, and as such, are often criticized for their simplicity. In this paper we attempt to address this latter issue by extending the ideas and findings of earlier studies to more complex coupled models in which one component is an Ocean General Circulation Model (OGCM). We will demonstrate that the optimal perturbation structures of hybrid coupled models are significantly influenced by atmospheric physics.

Our paper is laid out as follows. In section 2 we describe a hierarchy of coupled models that are used in the present study. In section 3 we examine the structure of the most unstable coupled ocean-atmosphere eigenmodes of each member of the model hierarchy, and explore the impact of atmospheric physics on the non-normality of the system. The optimal perturbations of each coupled model are examined in section 4 using various perturbation growth norms. We end with a discussion of our results and conclusions in section 5. An appendix introduces some important ideas relating to optimal perturbations using a simple illustrative example that will

be helpful for readers not familiar with the literature.

## 2 A Hierarchy of Coupled Models

Of interest in this study are the optimal perturbations of the primary modes of coupled ocean-atmosphere variability on seasonal-to-interannual timescales, both as potential triggers for low-frequency variability, such as ENSO episodes, and for generating ensemble forecasts. It could be argued that the most complete picture of these perturbations can only be obtained from Coupled ocean-atmosphere GCMs (CGCMs). While this may be true, the practicalities of computing the optimal perturbations using a CGCM are prohibitive because of the disparity in timescales between atmospheric instabilities, ocean instabilities, and low-frequency coupled ocean-atmosphere modes. To isolate the optimal perturbations of the low frequency coupled modes we have used simplified atmospheric models that describe only the low-frequency dynamics thought to be important for ENSO. These models do not support jets and fronts that yield very rapid perturbation growth at mid and upper levels of the troposphere on fast timescales (Molteni and Palmer, 1993; Buizza and Palmer, 1995; Hartmann *et al.*, 1995). Similar features in the ocean can also support optimal perturbation growth (Farrell and Moore, 1992; Moore and Farrell, 1993; Moore and Mariano, 1999), but a judicious choice of error growth norm can be used to focus attention on the lower frequency coupled modes of variability.

In this work we have used a hierarchy of three hybrid coupled models of ENSO. The hierarchical structure is determined by the complexity of the different atmospheric models used since the same OGCM is common to each coupled model. Our choice of models in the hierarchy was motivated by Moore and Kleeman (2001) who showed that atmospheric model physics have a significant impact on optimal perturbation structure in intermediate coupled models. The atmospheric models used in this study all emphasize a different aspect of air-sea interaction in the tropics. It is the impact of these different physical processes on the optimal perturbations that we have explored. Since all of the component models of our coupled model hierarchy are described elsewhere in detail, only a short description of each model is given here.

### 2.1 The Ocean Model

The ocean component common to each coupled model in the hierarchy is OPA 8.1, a primitive equation OGCM developed by Madec *et al* (1998). The version of the model used here is configured for the tropical Pacific Ocean between 120°E-75°W and 30°N-30°S, and is described in detail by Vialard and Delecluse (1998ab) and Vialard *et al.* (2001). The model horizontal resolution is 1° zonal, and increases in the meridional direction from 0.5° between 5°N-5°S to 2° at 30°N and 30°S. There are 25 levels in the vertical with 10 m thickness in the upper 150 m, and realistic bathymetry and coastal geometry are included.

Prior to coupling with each atmospheric model, the OGCM was first spun-up by forcing it with climatological monthly mean observed FSU winds for 30 years. The model was also forced by a surface heat flux  $Q = Q_h + \epsilon(T - T_r)$  where  $Q_h$  is the climatological seasonal cycle of surface heat flux derived from the ECMWF ReAnalysis (ERA),  $T$  is the model SST,  $T_r$  is the climatological mean observed seasonal cycle of SST from Reynolds and Smith (1994), and  $\epsilon = -40 \text{ W m}^{-2} \text{ K}^{-1}$  is a relaxation constant. A similar annual mean net freshwater flux forcing was used, composed of ERA net ( $E - P$ ) and a relaxation to the annual mean sea surface salinity of Levitus (1982). At the end of year 30 there are no significant long term trends in the upper ocean circulation within the 20°N-20°S band. Following this, the OGCM was then run for a further 40 years using the actual observed monthly mean FSU wind stress to force the model for the period 1960-1999. During this time, the observed climatological seasonal cycles of SST, surface heat flux and net surface freshwater flux derived from ERA, and annual mean Levitus surface salinity were also used to force the model.

## 2.2 Coupled Model 1

The first member of the coupled model hierarchy, referred to as Model 1, consists of the OGCM coupled to a statistical model of the atmosphere. The latter was constructed from a SVD analysis (Bretherton *et al.*, 1992) of the monthly mean SST anomalies of the OGCM and the monthly mean FSU wind stresses anomalies from the last 40 years of the OGCM spin-up described in section 2.1. Similar statistical atmospheric models have been used by others as reported in the literature (eg Latif and Villwock, 1990; Latif and Flügel, 1991; Balmaseda *et al.*, 1994; Syu *et al.*, 1995; Macias *et al.*, 1996; Kleeman *et al.*, 1999).

In Model 1 the OGCM was forced with a linear combination of the FSU monthly-mean climatological winds and the wind anomalies computed from the statistical atmospheric model in response to OGCM SST anomalies as illustrated schematically in Fig. 1a. The OGCM SST anomalies were computed relative to the 1967-1999 seasonal cycle of the OGCM spin-up experiment described in section 2.1.

## 2.3 Coupled Model 2

The second coupled model, referred to as Model 2, consists of the OGCM coupled to a 2-level dynamical model of the atmosphere. The atmospheric model is a steady state version of Kleeman (1989) in which the atmosphere is always assumed to be in steady state with the ocean SST (Kleeman, 1991), an excellent approximation in the tropics (Webster, 1972; Gill, 1980). The Kleeman atmospheric model is a global anomaly model, and computes the wind anomalies about the observed seasonal cycle which is specified from observations. The atmosphere is heated in two ways: (i) by Newtonian cooling/relaxation to the SST anomaly, which mimics the effects of sensible heat exchange, surface radiation and shallow convection, processes that are not explicitly represented in the model; and (ii) by latent heating due to deep penetrative convection via a simple moist static energy dependent convection scheme.

In Model 2, OGCM SST anomalies were computed as in Model 1 and passed to the atmospheric model as illustrated schematically in Fig. 1b. In response to these SST anomalies, the atmospheric model generates wind anomalies, and the OGCM is forced with a linear combination of these wind anomalies and the FSU monthly-mean climatological winds.

## 2.4 Coupled Model 3

The third member of the coupled model hierarchy, referred to as Model 3, consists of the OGCM coupled to the Kleeman atmospheric model via a model of the Atmospheric Boundary Layer (ABL) developed by Kleeman and Power (1995) (Fig. 1c). The ABL is a global anomaly model, and the potential temperature anomaly equation includes the effects of advection by the mean atmospheric circulation, turbulent heat transfer at the surface, and dissipation. The mean atmospheric circulation is prescribed from climatological observations, and the surface heat flux is computed using the normal bulk formula with stability dependent transfer coefficients. Complete details of the ABL are beyond the scope of this paper, and the reader is encouraged to consult Kleeman and Power (1995) who present a detailed description of the model and its performance.

In Model 3, the OGCM SST anomalies were computed as in Models 1 and 2. The resulting ABL temperature anomalies were computed relative to an ABL model seasonal cycle obtained by running the ABL for 30 years using observed monthly mean climatological surface temperatures. In Model 3, the net turbulent heat flux anomaly from the ABL was added to the climatological ERA fluxes described in section 2.1 and used to force the OGCM. The ABL temperature and specific humidity anomalies were used in the latent heat calculations for deep convection in the Kleeman atmospheric model. The wind stresses used to force the OGCM were

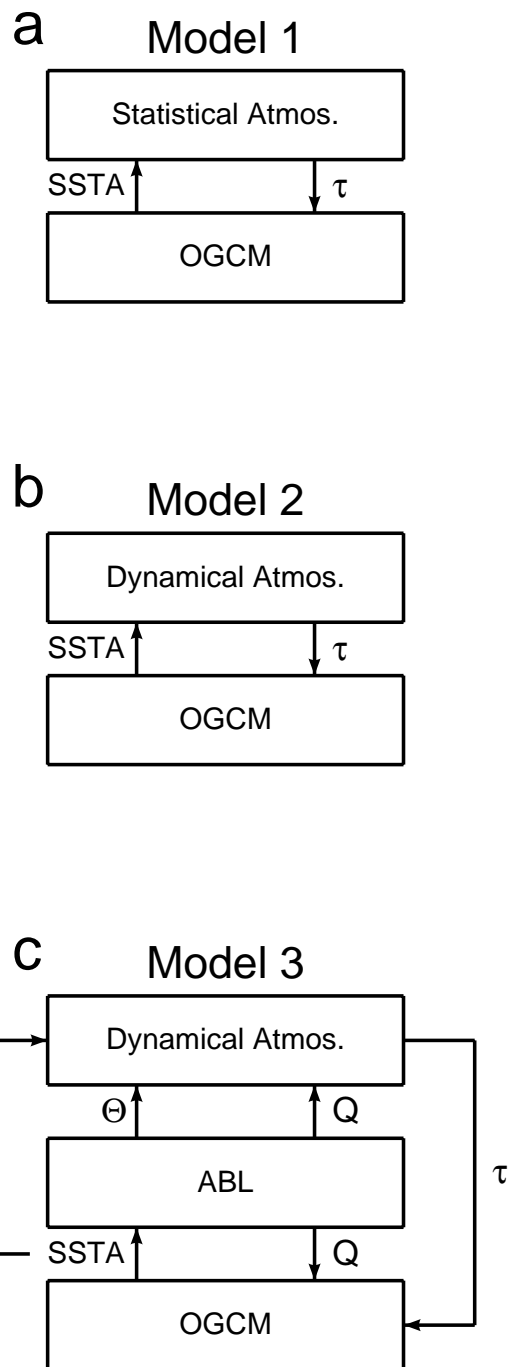


Figure 1: A schematic of each hybrid coupled model:  $\tau$  is the surface wind stress anomaly,  $\Theta$  is the ABL potential air temperature, and  $Q$  is the anomalous surface heat flux.

computed as in Model 2.

## 2.5 Coupled Model Performance

The efficacy of each coupled model was examined in terms of their ability to simulate variability on ENSO timescales by performing a series of hindcast experiments for the period 1980-1999, using the wind forced OGCM integration of section 2.1 as a surrogate for the truth. We use the OGCM solution in this way rather than the actual observed state of the coupled system because a data assimilation scheme was not available to properly initialize each model. Generally, it was found that each coupled model outperforms persistence, and exhibits a hindcast skill for SST that is comparable to several other models that are currently used for ENSO prediction.

## 3 Eigenmodes and Non-Normality

### 3.1 Eigenmode Structure

In sequel we will represent each coupled model symbolically as:

$$\frac{\partial \mathbf{S}}{\partial t} = N(\mathbf{S}) \quad (1)$$

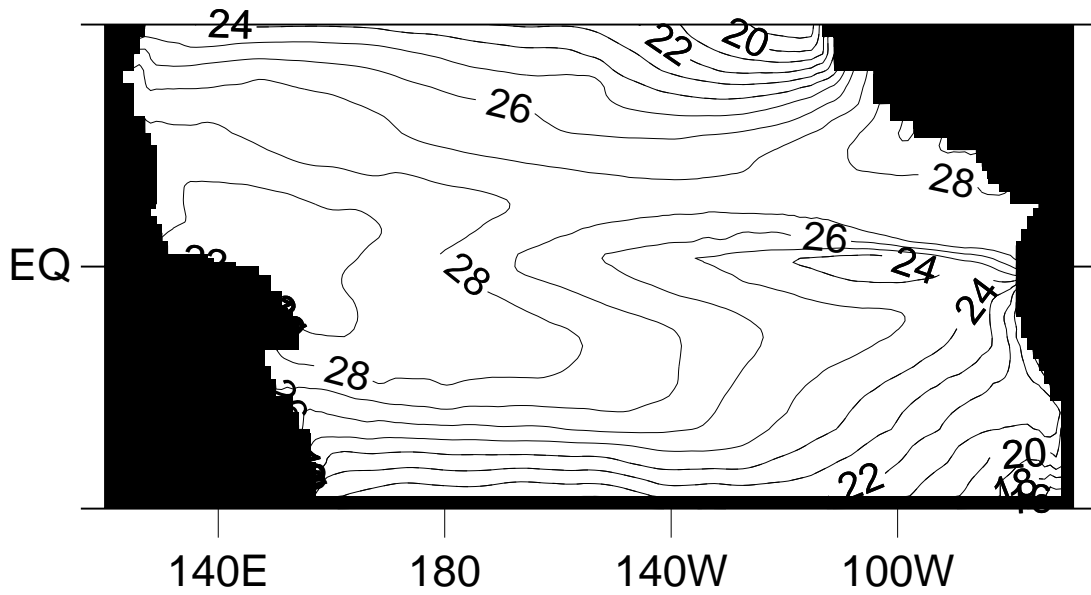
where  $\mathbf{S}$  represents the state-vector of the coupled system (*i.e.* the vector of model prognostic variables), and  $N$  collectively represents the operators that govern the time evolution of  $\mathbf{S}$ , some of which are non-linear.

We are interested in the evolution of small perturbations  $\mathbf{s}$  that are described by the tangent linear form of (1), namely  $\partial \mathbf{s} / \partial t = \mathbf{A} \mathbf{s}$  where  $\mathbf{A} = \partial N(\mathbf{S}) / \partial \mathbf{S} |_{\mathbf{S}_0}$ ,  $\mathbf{S}_0$  being a solution of (1) that is of particular interest.  $\mathbf{S}_0$  may be the actual time varying solution of (1), or it may be taken to represent the time mean trajectory. The latter is not strictly a solution of (1), but such approximations have been discussed and used extensively in the meteorological literature (eg Simmons and Hoskins, 1976; Frederiksen, 1982). In the present study, we will adopt this latter approach and concern ourselves with the case where  $\mathbf{S}_0$  does not vary in time. In this case the tangent linear equation is autonomous.

The vector  $\mathbf{S}_0$  will be referred to as the “basic state” and will represent the model annual mean conditions of the coupled system which were computed as the annual average of each model component forced separately with climatological observed boundary conditions. The ocean basic state is therefore identical in all models, and the SST and a vertical section of temperature along the equator are shown in Fig. 2 for future reference. A time independent basic state was used for two reasons: (i) to eliminate the influence that differences in the basic state of each coupled model, and its time evolution, may have on their eigenmode structures, and (ii) to simplify the analysis and dynamical interpretation of the resulting autonomous system. The eigenmodes and optimal perturbations of time-evolving basic states will be the subject of a future study.

For a time independent basic state, the eigenmodes are uniquely defined for all times, and as shown in the appendix, their properties are of interest. The eigenmodes of  $\mathbf{A}$  were computed iteratively using the tangent linear version of each coupled model and the ARPACK library of Lehoucq *et al.* (1997). Details of the tangent linear components of each model are given in Weaver *et al.* (2001) and Moore and Kleeman (1996), and the computational procedures are described in Appendix B of Moore *et al.* (2001).

a



b

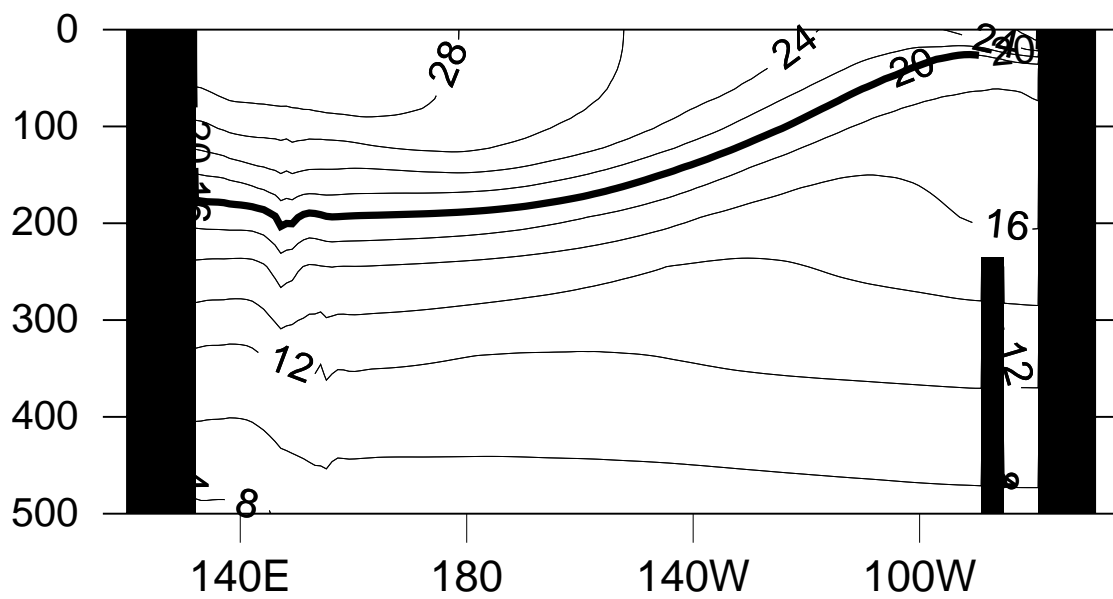


Figure 2: (a) The ocean basic state SST, and (b) a vertical section of the upper ocean temperature used for the eigenmode and optimal perturbation calculations. The contour interval is  $2^\circ$ .

The most unstable eigenmode of each coupled model takes the form of a low-frequency coupled ocean-atmosphere oscillation with a period and exponential growth rate that depends on the strength of the coupling between the atmosphere and ocean. In each coupled model the wind stress anomalies (and heat flux anomalies in Model 3) used to force the OGCM were multiplied by a factor  $\gamma$ , referred to as the “coupling strength.”

Model 1						Model 2				
$\gamma$	Period (yrs)	e-folding time (yrs)	$ v $	$\mu$	$e^{2\sigma\tau}$	Period (yrs)	e-folding time (yrs)	$ v $	$\mu$	$e^{2\sigma\tau}$
0.5									14	
0.8	3.6	0.7	24	127	4.6					
0.825						6.0	50	78	124	1.0
0.85						6.3	8.3	83		1.1
0.9						7.3	3.1	83		1.4
0.93						8.4	2.3	83		1.5
1.0	$\infty$	0.3	14	618	28.0	23.8	1.4	111	366	2.0

Table 1: A summary of the characteristics of the most unstable eigenmodes and optimal perturbations of Model 1 and Model 2 for various values of the coupling strength  $\gamma$ . For each model the following are given: the eigenmode period and e-folding growth time in years; the value of  $|v|$  defined in section 3.2 using the  $\mathcal{T}$  norm; the growth factor  $\mu$  of the fastest growing optimal perturbation for the  $\mathcal{T}$  norm for an optimal growth time of  $\tau = 6$  months; and the energy growth factor  $e^{2\sigma\tau}$  of a perturbation with structure of the most unstable eigenmode, where  $\sigma$  is the eigenmode growth rate. Blank entries indicate values that were not computed.

Table 1 shows how the period and e-folding time of the most unstable eigenmode of Models 1 and 2 vary with  $\gamma$ , and indicates that the period (e-folding time) increases (decreases) with increasing  $\gamma$ . No eigenmode solutions could be found using ARPACK for any of the models for values of  $\gamma$  below the primary bifurcation point. For Model 2 this occurs around  $\gamma = 0.8$ . Model 3 exhibits qualitatively similar behaviour to Models 1 and 2, and all models generally agree with the behaviour of the coupled ocean-atmosphere modes discussed by Jin and Neelin (1993ab) and Neelin and Jin (1993). The following values of  $\gamma$  were used in all remaining calculations: Model 1,  $\gamma = 0.8$ ; Model 2,  $\gamma = 0.825$ ; Model 3,  $\gamma = 1.0$ . These values of  $\gamma$  yield unstable eigenmodes with similar oscillation frequencies in each model, and as close as we could find to the observed frequency range of ENSO. The eigenmode of Model 2 is the lowest frequency mode that could be identified in the present study.

The real and imaginary components of SST for the most unstable eigenmode of each coupled model are shown in Fig. 3. These fields represent the SST structure of the eigenmodes separated by one quarter of a period. The associated period and exponential growth rate of each eigenmode is indicated, and the basic state SST is shown in Figs. 2a for reference. The SST structure of the Model 3 eigenmode is very similar to that of Model 2 and is not shown. Instead, the ABL potential temperature anomaly  $\theta$  of the Model 3 eigenmode is shown in Figure 3ef. For each model, the ocean temperature structure of each eigenmode has a significant amplitude only down to the depth of the thermocline (not shown).

The eigenmode of Model 1 (Fig. 3ab) takes the form of an oscillation with a period of 3.61 years. The eigenmode is “ENSO-like” in SST and takes the form of a standing wave in the east Pacific which is more clearly illustrated in Figs. 4ab which shows a Hovmöller diagram of SST and zonal wind stress anomalies averaged between  $2^\circ\text{N}$  and  $2^\circ\text{S}$ .

The eigenmode of Model 2 (Fig. 3cd) takes the form of an oscillation with a period of 6 years with a predominantly dipole structure in SST along the equator. The west Pacific node of the dipole over the warm pool is associated with deep convection in the Kleeman atmospheric model. This eigenmode takes the form of a

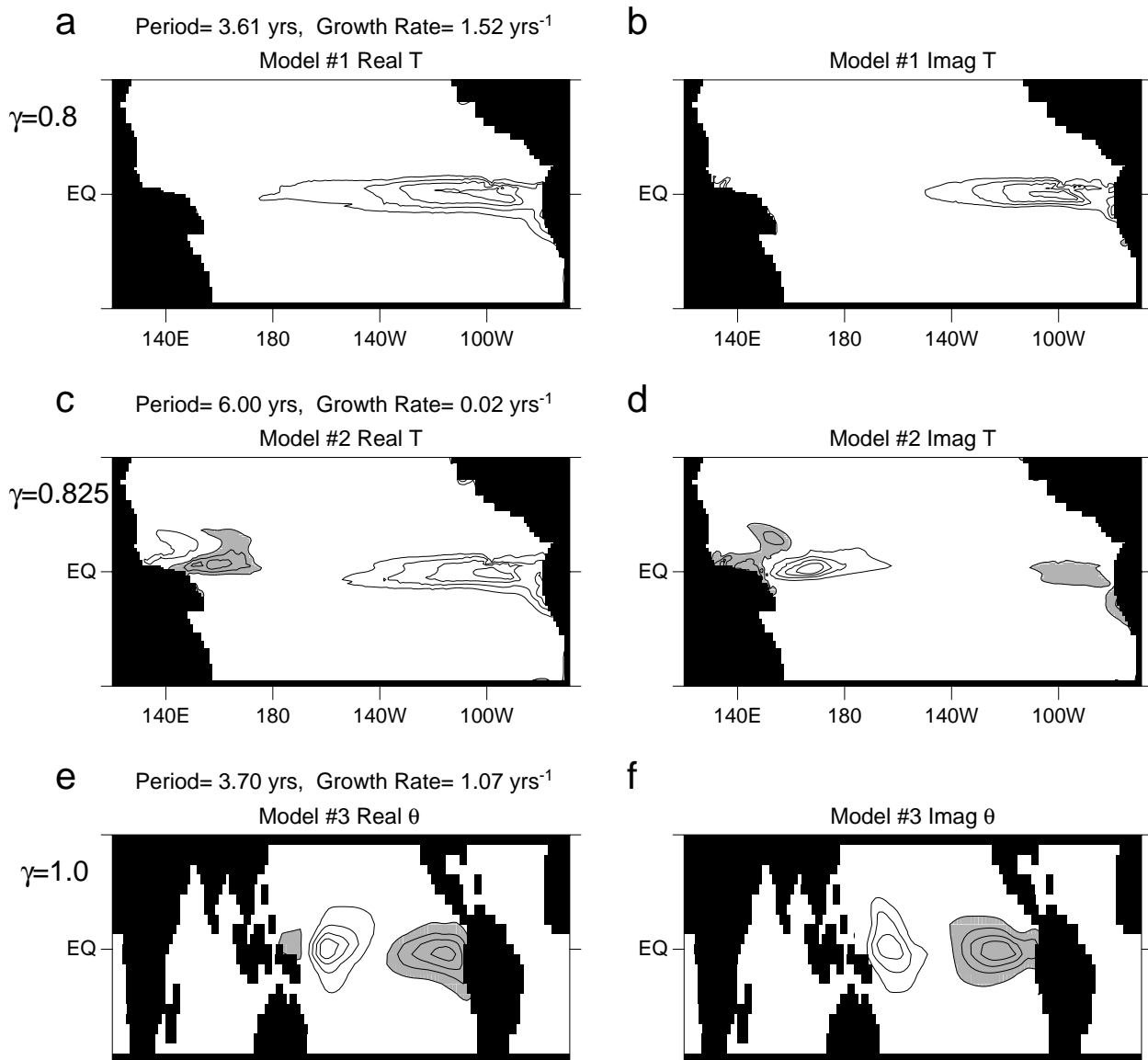


Figure 3: The real and imaginary components of SST for the most unstable eigenmode of (a,b) Model 1, and (c,d) Model 2. The ABL temperature anomaly of Model 3 is shown in (e,f) for the entire ABL model domain. The period and growth rate of the eigenmode is also indicated. Shaded and unshaded regions indicate perturbations of the opposite sign. The contour interval is arbitrary.

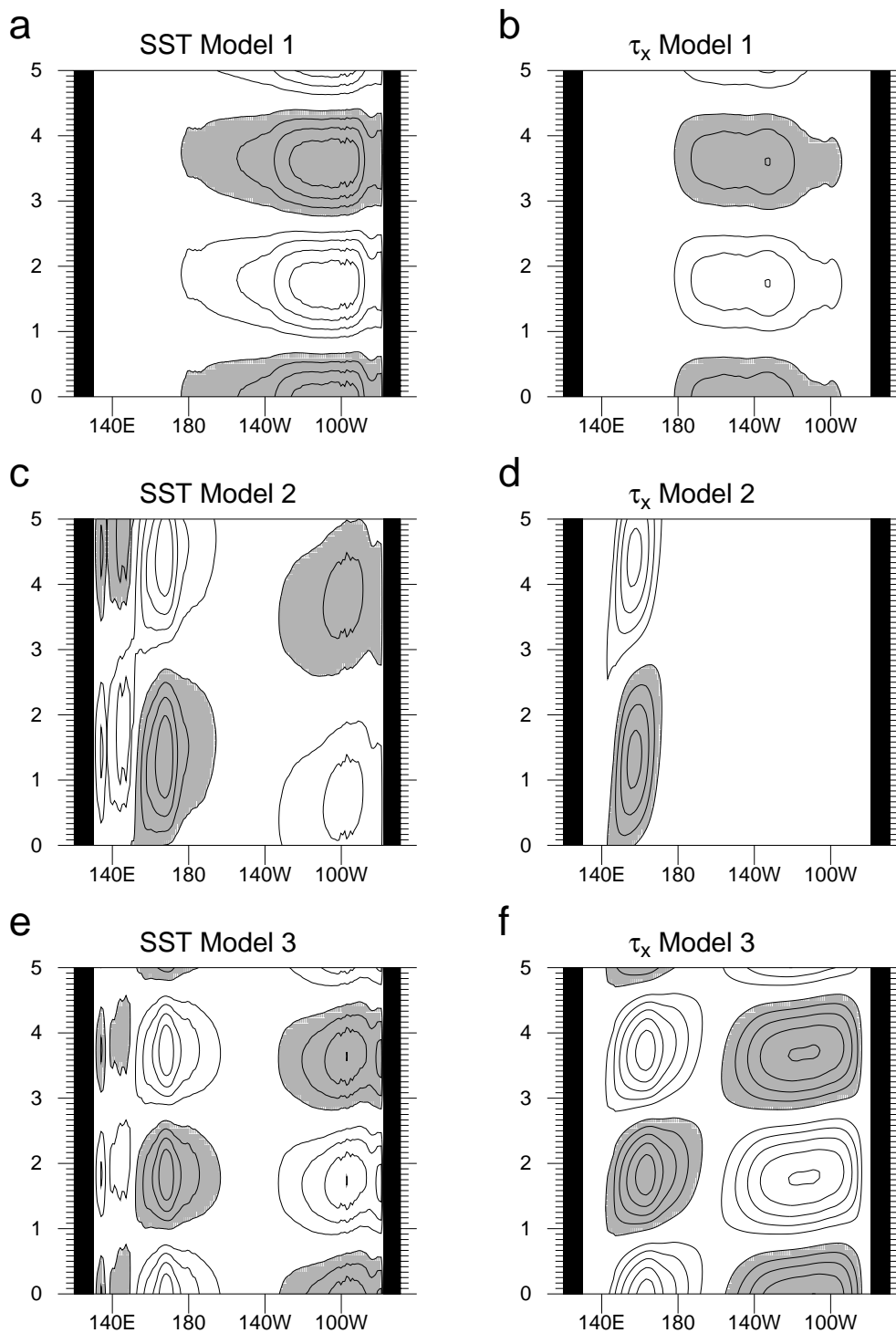


Figure 4: Hovmöller diagrams of SST and zonal wind stress  $\tau_x$  averaged between  $2^\circ\text{N}$  and  $2^\circ\text{S}$  for the most unstable eigenmode of (a,b) Model 1, (c,d) Model 2, and (e,f) Model 3. Shaded and unshaded regions indicate perturbations of opposite sign. The contour interval is arbitrary. In each case the exponential growth of the eigenmodes has been suppressed.

standing wave as shown in Fig. 4cd.

The ABL temperature fields for the Model 3 eigenmode are shown in Fig. 3ef, and reflect the SST anomalies. The eigenmode of Model 3 takes the form of an oscillation with a period of 3.7 years as shown in Figs. 4ef.

The SST structure of the Model 1 eigenmode is qualitatively similar to the first EOF of the observed SST (see Fig. 8 of Palmer and Anderson, 1994), while the SST structures of the eigenmodes of Models 2 and 3 are reminiscent of the 2nd EOF. Thus each coupled model captures some aspects of the observed modes of SST variability, and describes a subset of the atmospheric dynamics thought to be important for air-sea interaction in the tropical Pacific on seasonal to interannual timescales. The perturbation dynamics of each model may therefore provide valuable information about the potential influence of each atmospheric process on the non-normality of the coupled system, and the potential impact on perturbation growth in nature and in complex CGCMs.

### 3.2 Adjoint Eigenmode Structure

As discussed in the appendix, the structure and properties of optimal perturbations depend on the degree of linear dependence of the eigenmodes of  $\mathbf{A}$  (Farrell, 1982, 1984, 1985, 1988ab, 1989ab). If  $\mathbf{A}$  is normal, its eigenmodes are orthogonal and the optimal perturbations coincide with the eigenmodes. On the otherhand, if  $\mathbf{A}$  is non-normal, which is usually the case, the eigenmodes are linearly dependent. The degree of linear dependence is one factor that determines the structure and growth of the resulting optimal perturbations (Farrell and Ioannou, 1996).

We will denote the most unstable eigenmode of each coupled model as  $\mathbf{e}$ , and the corresponding adjoint eigenmode as  $\mathbf{b}$ . The adjoint operator and adjoint eigenmodes are by definition norm dependent (Courant and Hilbert, 1953). To see this, suppose we denote by  $\langle \mathbf{v}, \mathbf{u} \rangle$  the inner-product  $\mathbf{v}^T \mathbf{X} \mathbf{u}$  where  $\mathbf{X}$  is a symmetric positive definite matrix. The adjoint of  $\mathbf{A}$  with respect to this inner-product is found by noting that  $\mathbf{X} = \mathbf{X}^T$  and  $\langle \mathbf{v}, \mathbf{A} \mathbf{u} \rangle = \mathbf{v}^T \mathbf{X} \mathbf{A} \mathbf{u} = \mathbf{u}^T \mathbf{A}^T \mathbf{X}^T \mathbf{v} = \mathbf{u}^T \mathbf{X} (\mathbf{X}^{-1} \mathbf{A}^T \mathbf{X}) \mathbf{v} = \langle \mathbf{u}, (\mathbf{X}^{-1} \mathbf{A}^T \mathbf{X}) \mathbf{v} \rangle$ . Thus the adjoint of  $\mathbf{A}$  with respect to the chosen norm is  $\mathbf{X}^{-1} \mathbf{A}^T \mathbf{X}$ . The adjoint of  $\mathbf{A}$  with respect to the L2-norm ( $\mathbf{X} = \mathbf{I}$ ) is therefore  $\mathbf{A}^T$ . If  $\mathbf{b}$  is an eigenvector of  $\mathbf{A}^T$ , then  $\mathbf{X}^{-1} \mathbf{b}$  is an eigenvector of the adjoint  $\mathbf{X}^{-1} \mathbf{A}^T \mathbf{X}$ . In sequel the adjoint eigenmodes  $\mathbf{b}$  are the eigenvectors of the adjoint operator relative to the L2-norm. In this regard, the adjoint eigenmodes are also of interest because they represent the optimal excitation of the corresponding eigenmodes of  $\mathbf{A}$  which yield the most rapid growth of the norm  $\mathbf{v}^T \mathbf{X} \mathbf{u}$ .

A useful quantitative measure of the degree of linear dependence of  $\mathbf{e}$  on the remaining eigenmodes of  $\mathbf{A}$  is given by  $v = |\mathbf{G} \mathbf{b}| |\mathbf{G}^T \mathbf{e}| / (\mathbf{b}^T \mathbf{G} \mathbf{G}^T \mathbf{e})$  (Farrell and Ioannou, 1999), where  $\mathbf{X} = \mathbf{G} \mathbf{G}^T$ , and  $\mathbf{G} = \mathbf{I}$  for the L2-norm (see appendix). Since  $\mathbf{e}$  and  $\mathbf{b}$  are complex vectors,  $v$  will also in general be complex so we consider  $|v|$ .

The most unstable adjoint eigenmodes  $\mathbf{b}$  of each coupled model were computed using the adjoint versions of each tangent linear coupled model (Weaver *et al.*, 2001; Moore and Kleeman, 1996). The SST structure of the most unstable adjoint eigenmodes for each coupled model are shown in Fig. 5.

For Model 1, the adjoint eigenmode takes the form of a dipole spanning the entire equatorial Pacific (Figs. 5ab). A Hovmoller diagram of the equatorial adjoint eigenmode SST is shown in Fig. 6a confirming that the period is identical to that of the corresponding eigenmode (cf Fig. 4a). The values of  $|v|$  for the Model 1 eigenmode for two norms relevant to later sections of the paper are shown in Table 2.

In the case of Model 2, Figs. 5cd show that the adjoint eigenmode is confined mainly to the west Pacific warm pool. Figure 6b shows a Hovmoller plot of the adjoint eigenmode equatorial SST. The values of  $|v|$  for the eigenmode of Model 2 are shown in Table 2, and a comparison with those of Model 1 reveals that the most unstable eigenmode of Model 2 is more non-normal than that of Model 1. This is in agreement with

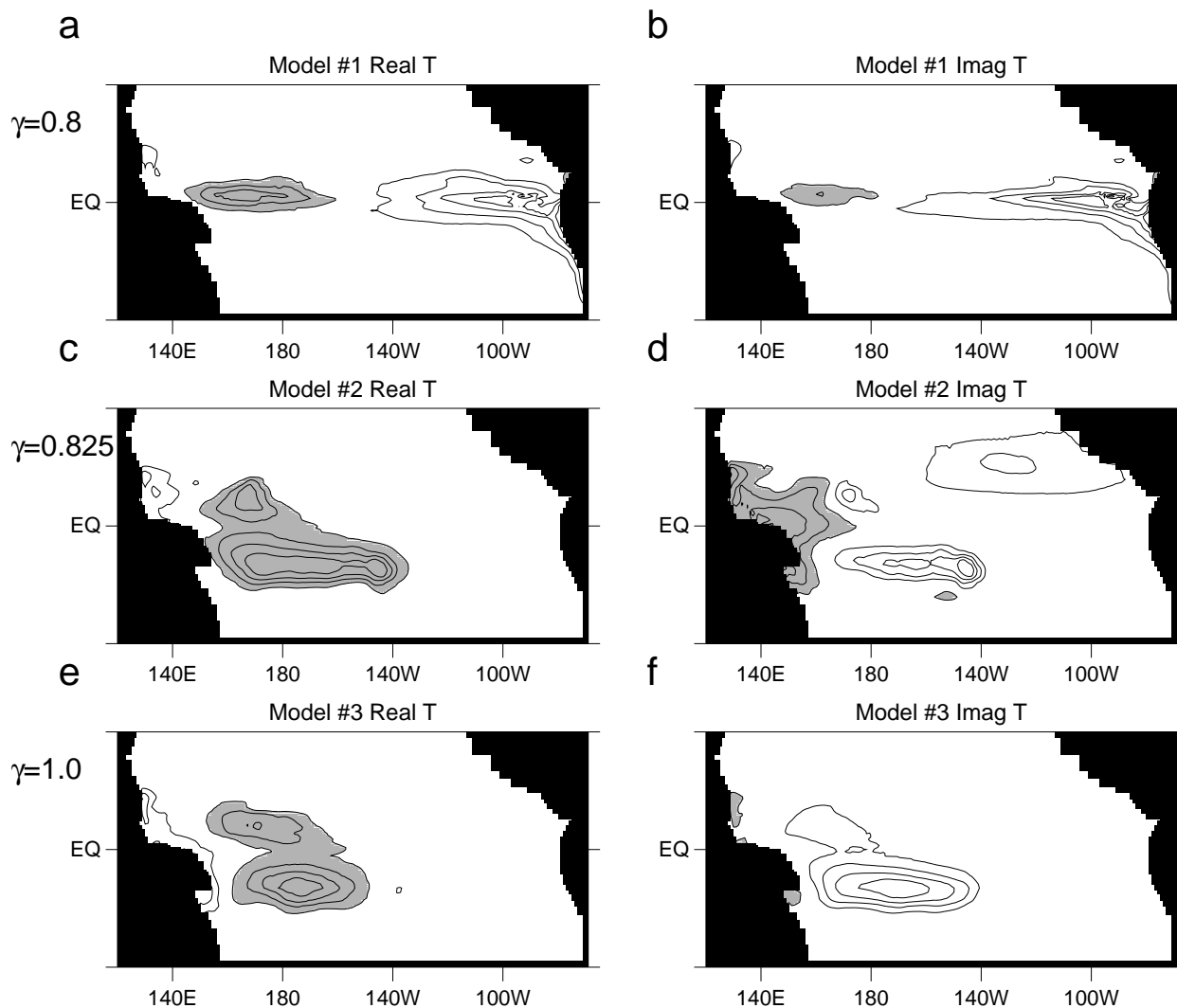


Figure 5: The real and imaginary components of SST of the most unstable adjoint eigenmode for (a,b) Model 1, (c,d) Model 2, and (e,f) Model 3. Shaded and unshaded regions indicate perturbations of opposite sign. The contour interval is arbitrary.

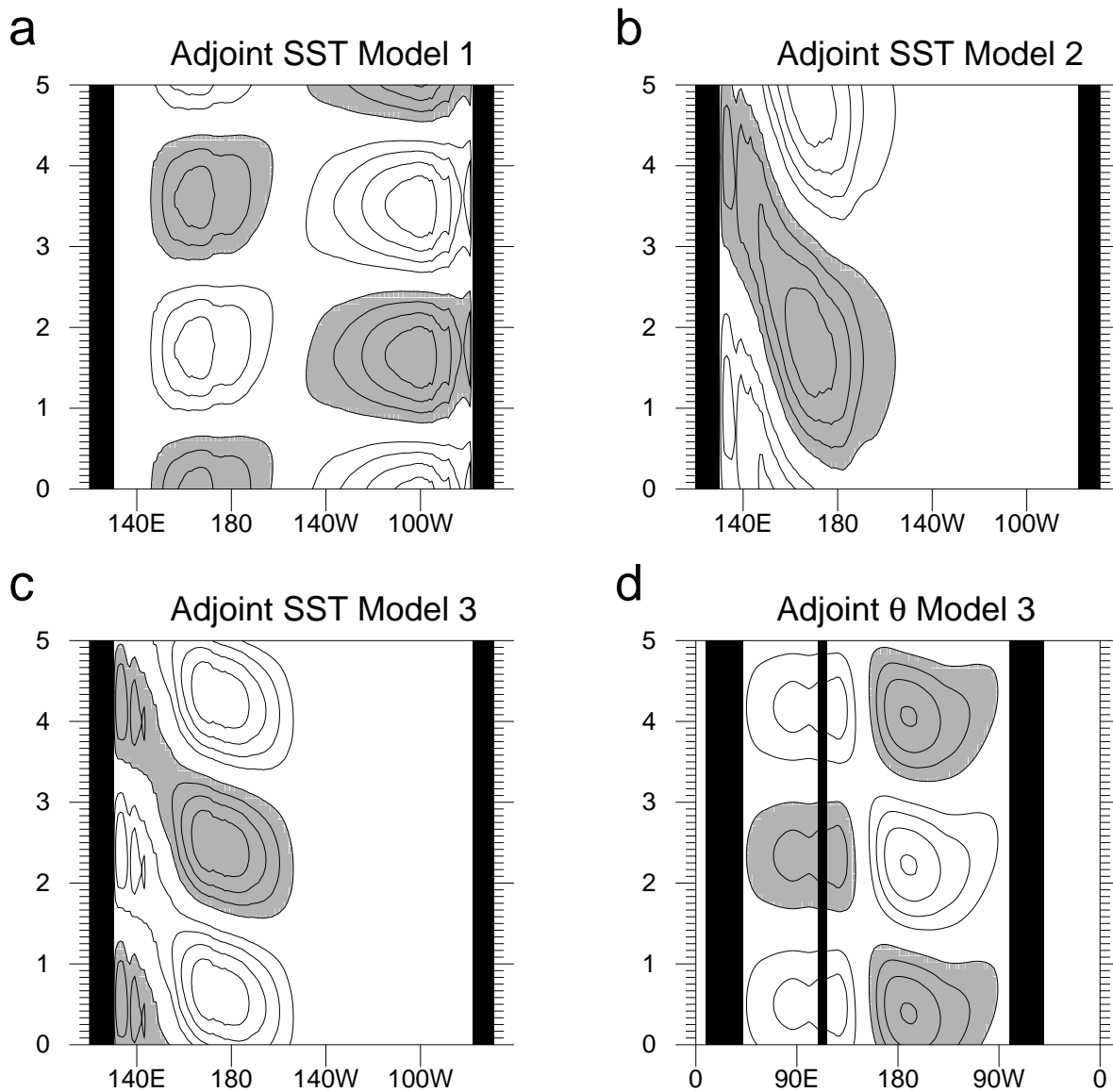


Figure 6: Hovmoller diagrams of SST averaged between  $2^{\circ}\text{N}$  and  $2^{\circ}\text{S}$  for the most unstable adjoint eigenmode of (a) Model 1, (b) Model 2, and (c) Model 3. (d) A Hovmoller diagram of ABL  $\theta$  averaged between  $2^{\circ}\text{N}$  and  $2^{\circ}\text{S}$  for the most unstable adjoint eigenmode of Model 3 for the entire longitudinal domain of the ABL. Shaded and unshaded regions indicate perturbations of opposite sign. The contour interval is arbitrary. In each case the exponential growth of the eigenmodes has been suppressed.

	Model 1	Model 2	Model 3
L2-Norm	211	450	479
$\mathcal{T}$ -Norm	24	78	83

Table 2: The values of  $|\nu|$  where  $\nu = |\mathbf{G}\mathbf{b}| |\mathbf{G}^T \mathbf{e}| / (\mathbf{b}^T \mathbf{G} \mathbf{G}^T \mathbf{e})$  where  $\mathbf{e}$  denotes the most unstable oscillatory eigenmode and  $\mathbf{b}$  is the corresponding adjoint eigenmode. Values of  $|\nu|$  are shown for the most unstable oscillatory eigenmodes of each coupled model using two different norms defined by  $\mathbf{G}$ . Please see the main text for the appropriate definitions of  $\mathbf{G}$  in each case.

the findings of Moore and Kleeman (2001) who showed that the deep convection over the warm pool in the Kleeman atmospheric model can significantly increase the non-normality of the system.

For Model 3, Figs. 5ef and Fig. 6c show that the adjoint eigenmode is similar to that of Model 2. A Hovmoller diagram of the adjoint ABL  $\theta$  is shown in Fig. 6d, and reveals that SST and  $\theta$  are  $180^\circ$  out of phase over the warm pool. The values of  $|\nu|$  for the most unstable eigenmode of Model 3 are shown in Table 2 which reveals that of all three models, Model 3 is the most non-normal. We will comment further on the structure of the adjoint eigenmodes in section 4 when we present the optimal perturbations.

The general structure of the most unstable eigenmodes and adjoint eigenmodes of each model are insensitive to variations in the coupling strength  $\gamma$ . On the otherhand the values of  $|\nu|$  for these eigenmodes do exhibit a sensitivity to  $\gamma$  as shown in Table 1. For Model 1  $|\nu|$  decreases as  $\gamma$  increases, while for Model 2  $|\nu|$  generally increases with  $\gamma$ .

## 4 Optimal Perturbations of the Annual Mean State

The optimal perturbations of each coupled model with respect to the norm  $\mathcal{N} = \mathbf{s}^T \mathbf{G} \mathbf{G}^T \mathbf{s}$  are, by definition, the right singular vectors of  $\mathbf{G}^T \mathbf{R}(\tau)$  where  $\mathbf{R}(\tau)$  is the propagator of the tangent linear equation (see appendix),  $\tau$  is the optimal growth time, and  $\mathbf{G}$  defines the norm used to measure perturbation growth. The squares of the corresponding singular values represent the growth factor  $\mu$  of  $\mathcal{N}$  for the optimal perturbations over the time interval  $\tau$ . The growth factor  $\mu$  can be written as:

$$\mu = \mathbf{s}^T(0) \mathbf{R}^T(\tau) \mathbf{G} \mathbf{G}^T \mathbf{R}(\tau) \mathbf{s}(0) / \mathbf{s}^T(0) \mathbf{G} \mathbf{G}^T \mathbf{s}(0) \quad (2)$$

and equation (2) verifies that the optimal perturbations are the eigenvectors of  $\mathbf{R}^T(\tau) \mathbf{G} \mathbf{G}^T \mathbf{R}(\tau)$ . In general, the norms used at initial and final time can be different as is often the case in numerical weather prediction where the analysis error covariance is used to define  $\mathbf{G}$  at initial time (Fan *et al.*, 2000; Barkmeijer *et al.*, 1998). As in section 3 we will confine our attention to autonomous systems where (1) was linearized about an annual mean state of each model, recalling that the ocean basic state is identical for all three models. As noted in section 3, this assumption greatly simplifies the analysis and interpretation of the optimal perturbations. For Models 1 and 2, the state vector  $\mathbf{s} = (T, S, u, v)^T$  where  $T$  and  $S$  are the temperature and salinity perturbations, and  $(u, v)$  are the ocean current perturbations. For Model 3,  $\mathbf{s} = (T, S, u, v, \theta)^T$  where  $\theta$  is the boundary layer perturbation potential temperature.

The singular vectors with respect to two different norms will be considered. The first norm is relevant to the problem of error growth in ENSO forecast models, while the second is of general dynamical interest.

#### 4.1 A Temperature Norm

The first norm considered as a measure of perturbation growth is the basin-integrated squared temperature perturbation denoted  $\mathcal{T}$  and defined as:

$$\mathcal{T} = \int_{-H(\lambda, \varphi)}^0 \int_{\lambda_w}^{\lambda_e} \int_{\varphi_s}^{\varphi_n} T^2 a \cos \varphi d\lambda d\varphi dz \quad (3)$$

where  $H(\lambda, \varphi)$  is the spatially varying depth of the ocean,  $\lambda_w \equiv \lambda_w(\varphi)$  and  $\lambda_e \equiv \lambda_e(\varphi)$  define the longitude of the western and eastern boundaries respectively,  $\varphi_s$  and  $\varphi_n$  are the northern and southern latitudes of the model domain, and  $a$  is the Earth radius. This norm is representative of the type of norm that would be of interest for ENSO prediction, and in this example would represent the temperature errors of a model forecast. The depth, latitude and longitude ranges in (3) may be tailored for specific needs, but we consider the entire ocean domain. For  $\mathcal{T}$ , all elements of  $\mathbf{G}$  in (2) are zero except the first  $N_o$  diagonal elements, where  $N_o$  is the number of ocean temperature grid points. At initial time  $S = u = v = \theta = 0$  at all latitudes, longitudes and depths, and  $\tau = 6$  months.

The  $\mathcal{T}$  growth factors of the first 10 members of the optimal perturbation spectrum of each coupled model are shown in Fig. 7. In each case, the spectrum is dominated by the first member, which is in agreement with the optimal perturbation spectra of intermediate coupled models cited in section 1. For comparison, the optimal perturbation spectrum of the OGCM alone ( $\gamma = 0$ ) using the same basic state is also shown in Fig. 7, and in contrast to the coupled models, is very flat. The initial and final SST structures of the fastest growing optimal perturbation of each coupled model are shown in Fig. 8.

For Model 1, Fig. 8a shows that the fastest growing optimal perturbation (hereafter referred to as OP1) has an initial SST structure in the form of a dipole spanning the entire basin. The amplitude of the initial temperature perturbation is significant only down to the depth of the thermocline, as shown in Fig. 9a. The westward extension of the subsurface temperature perturbation along the thermocline evident in Fig. 9a is consistent with the recent adjoint sensitivity experiments of Galanti *et al.* (2001) using a similar hybrid coupled model.

The initial SST structure of OP1 is remarkably similar to the real phase of the most unstable adjoint eigenmode of Model 1 shown in Fig. 5a. Figure 8b shows that OP1 evolves into an ENSO-like episode, which has a structure similar to the real phase of the most unstable eigenmode of Model 1 (cf Fig. 3a). Thus OP1 is optimal for exciting the most unstable coupled ocean-atmosphere eigenmode of the system. The similarity between OP1 and the adjoint eigenmode was anticipated because, as noted in section 3.2, the adjoint eigenmode is the optimal excitation for the corresponding eigenmode, and at the same time maximises the growth of the norm associated with the inner-product that defines the adjoint operator. In this case the adjoint operator was defined with respect to the L2-norm, and the  $\mathcal{T}$ -norm is a subset of the L2-norm. The growth factor of  $\mathcal{T}$  for OP1 is 127. However, a perturbation with the structure of the most unstable eigenmode would grow by a factor of  $e^{2\sigma\tau}$ , where  $\sigma$  is the real part of its eigenvalue. According to Table 1, a perturbation with this structure would grow in Model 1 by only a factor of 4.6 over a 6 month period. Thus the growth of OP1 over and above that expected for the most unstable eigenmode must be due to the interference of the non-normal eigenmodes of the system.

Figures 8cd show that the SST structure of OP1 for Model 2 is confined primarily to the west Pacific warm pool. As in Model 1 the amplitude of OP1 is significant only above the thermocline (Figs. 9cd), and OP1

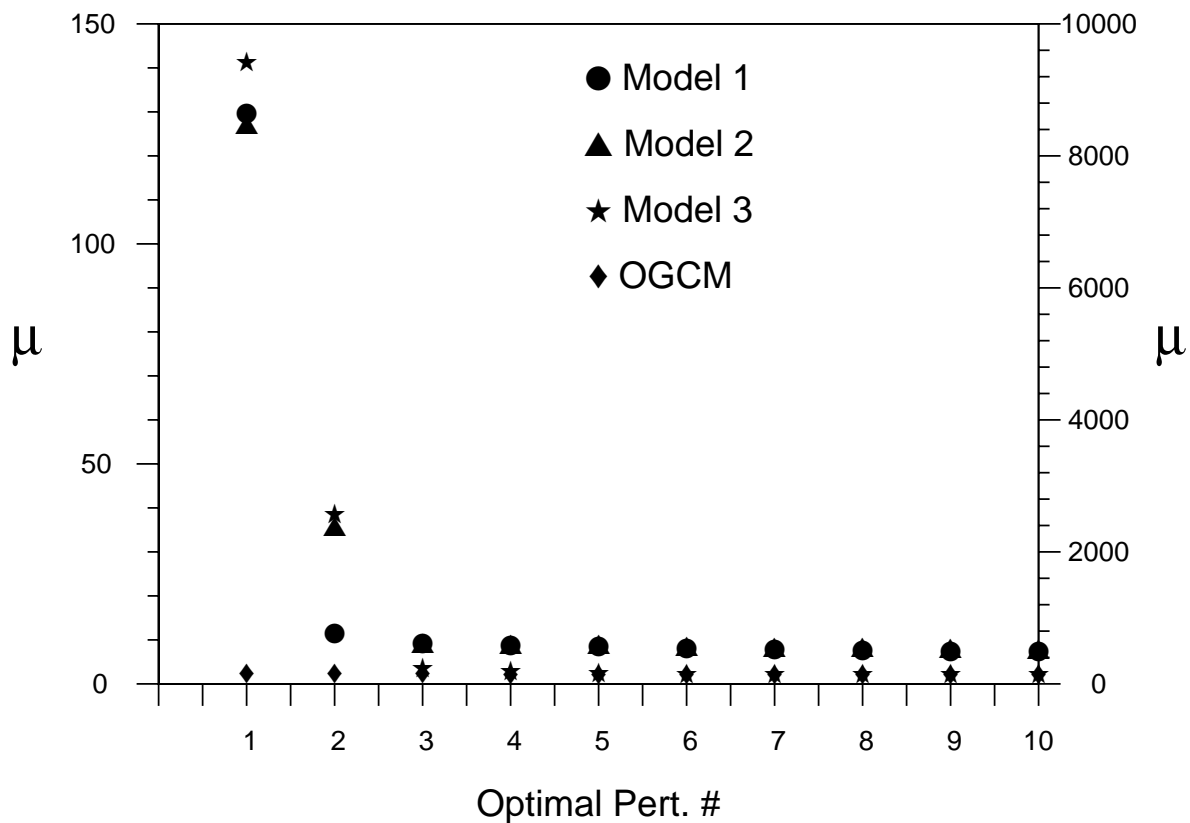


Figure 7: The growth factor  $\mu$  of the  $\mathcal{T}$  norm for the first 10 members of the optimal perturbation spectrum of each coupled model and the OGCM ( $\gamma = 0$ ) for  $\tau = 6$  months. The left ordinate is for Models 1 and 2 and the OGCM, and the right ordinate is for Model 3.

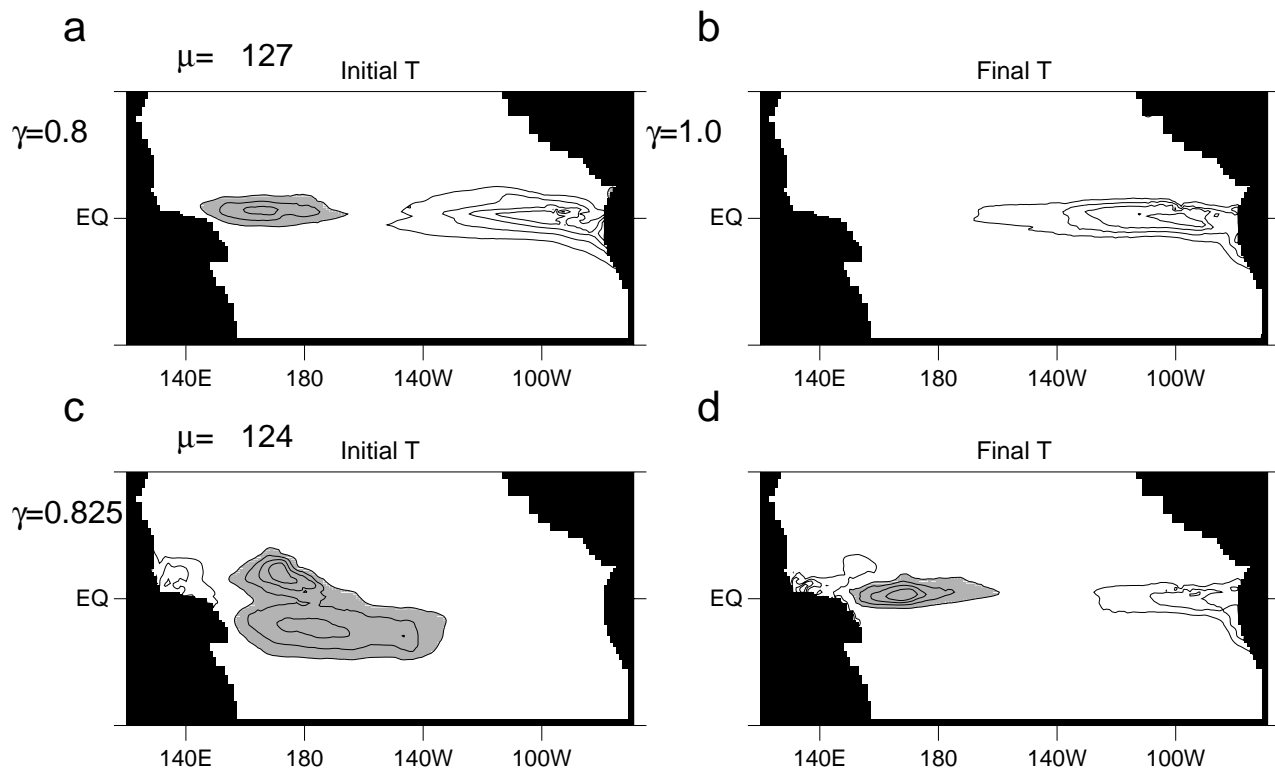


Figure 8: The SST structure of the fastest growing optimal perturbations of (a,b) Model 1, and (c,d) Model 2 using the  $\mathcal{T}$  norm for  $\tau = 6$  months. The contour interval is arbitrary, and the growth factor  $\mu$  of  $\mathcal{T}$  is indicated.

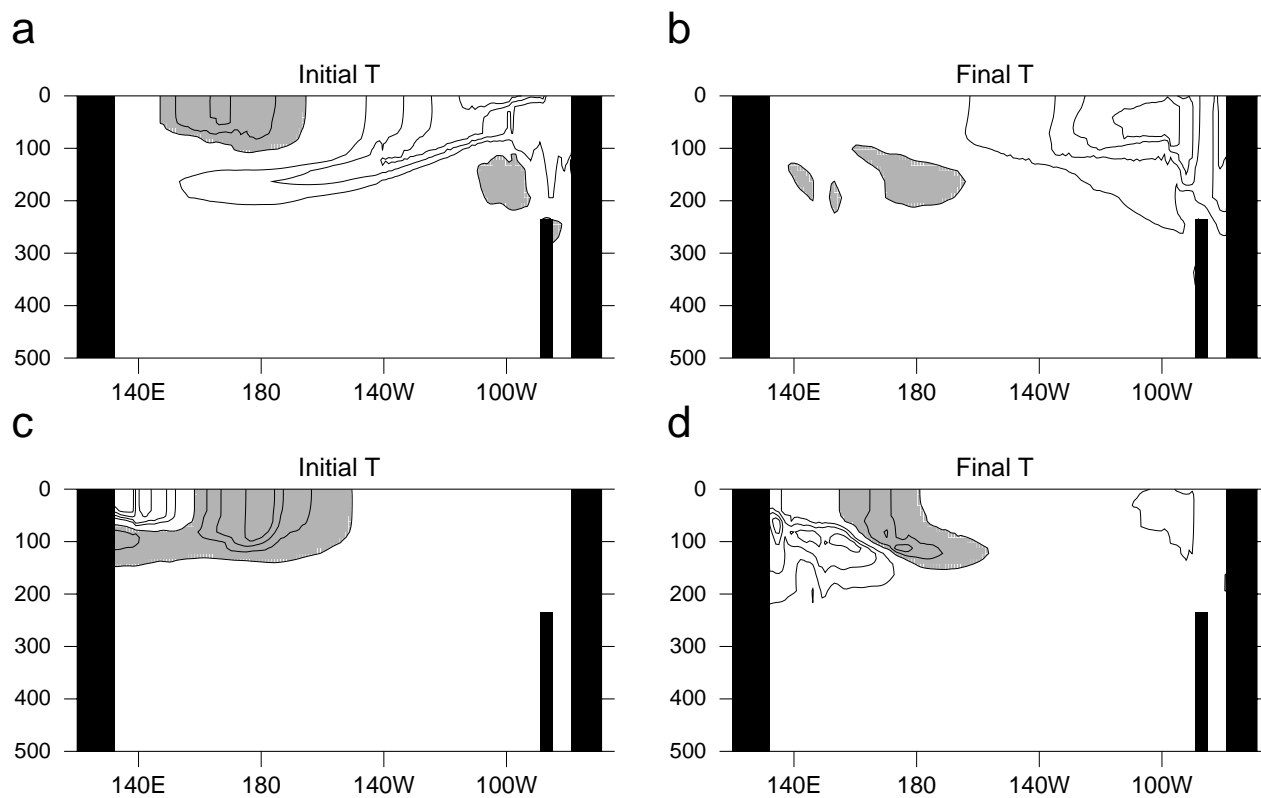


Figure 9: Vertical sections of ocean temperature along the equator at initial and final time are shown in (a,b) for Model 1, and (c,d) for Model 2. Shaded and unshaded regions indicate perturbations of opposite sign. The contour interval is arbitrary.

bears a remarkable resemblance to the real phase of the most unstable adjoint eigenmode of Model 2 shown in Fig. 5c. Figure 8d reveals that the Model 2 OP1 evolves into a perturbation that is strikingly similar to the real phase of the most unstable eigenmode (cf Fig. 3c). Thus OP1 of Model 2 is also optimal for exciting the most unstable coupled ocean-atmosphere eigenmode. The growth factor of  $\mathcal{T}$  for OP1 is 124, but from Table 1, a perturbation with the structure of the most unstable eigenmode would grow by only a factor of 1.02 over a 6 month period. The growth of OP1 over and above that for the most unstable eigenmode is due to the interference of the non-orthogonal eigenmodes of Model 2.

The SST structure of OP1 for Model 3 is very similar to that of Model 2 and is not shown. However, the growth factor of  $\mathcal{T}$  for OP1 in Model 3 is 9286, some 74 times larger than that of Models 1 and 2. A perturbation with the structure of the most unstable eigenmode would grow by only a factor of 2.9. Thus the greatly increased growth factor of the Model 3 OP1 is due to the higher degree of non-normality of the most unstable eigenmode compared to the corresponding eigenmodes of Models 1 and 2 (see Table 2).

The same OP growth factor can be obtained for a range of eigenvalues and values of  $\nu$  as shown in the appendix. Table 1 shows evidence for this in Models 1 and 2 which have similar OP growth factors for  $\mathcal{T}$  despite differences in  $\gamma$  and the period, growth rate and  $|\nu|$  for their most unstable eigenmodes. Table 1 also reveals that a different choice of  $\gamma = 1$  yields very disparate OP growth factors for  $\mathcal{T}$  with that of Model 1 being larger despite the fact that the Model 2 eigenmode is more non-normal than the Model 1 eigenmode. We also note that like the example in the appendix, OP growth is also possible when there are no growing eigenmodes. Table 1 reveals that OP1 of Model 2 still grows when  $\gamma = 0.5$  which Table 1 suggests is well below the primary bifurcation point for this model.

For Model 3, an additional temperature-based norm was considered:

$$\mathcal{T}' = \mathcal{T} + h_0 \int_0^{2\pi} \int_{\phi_s}^{\phi_n} \theta^2 a \cos \phi d\lambda d\phi \quad (4)$$

which represents  $\mathcal{T}$  plus the domain-integrated squared ABL perturbation temperature, and  $h_0$  is the boundary layer thickness. As before  $S = u = v = 0$  for the ocean at initial time, but now  $\theta \neq 0$ . The fastest growing optimal perturbation of Model 3 for the  $\mathcal{T}'$  norm is shown in Fig. 10 and is virtually identical to that for the  $\mathcal{T}$ -norm. The growth factor of  $\mathcal{T}'$ , however, is larger than that of  $\mathcal{T}$  for the same optimal growth time, and is achieved by initial temperature differences between the sea surface and ABL. Figure 10 shows that at initial time, perturbations in SST and  $\theta$  are of opposite sign in the western Pacific, which enhances the air-sea heat exchange. This behavior is consistent with the  $180^\circ$  phase difference between the SST and  $\theta$  anomalies of the most unstable adjoint eigenmode in Figs. 6cd. An intermediate coupled model composed of the same atmosphere as Model 3 but with a simplified ocean (Kleeman, 1993) shows qualitatively similar behaviour (not shown) confirming the controlling influence that the ABL dynamics have on the optimal perturbation structure.

## 4.2 Dynamics of $\mathcal{T}$ Optimals

The time evolution of  $\mathcal{T}$  is given by:

$$\mathcal{T}(t) = \mathcal{T}(0) - \underbrace{2 \int_0^t \int_V \frac{uT}{a \cos \phi} \frac{\partial \bar{T}}{\partial \lambda} dV dt}_A - \underbrace{2 \int_0^t \int_V \frac{vT}{a} \frac{\partial \bar{T}}{\partial \phi} dV dt}_B - \underbrace{2 \int_0^t \int_V wT \frac{\partial \bar{T}}{\partial z} dV dt}_C$$

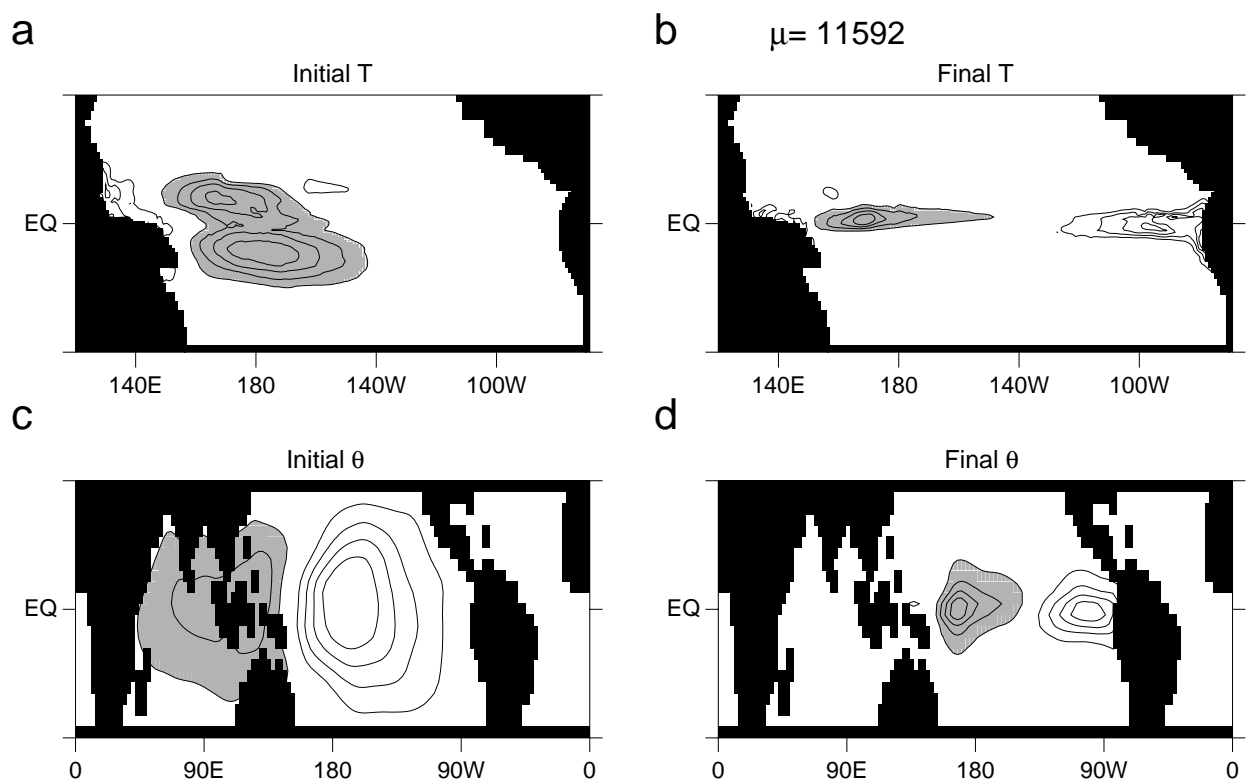


Figure 10: The fastest growing optimal perturbation of Model 3 using the  $\mathcal{T}'$  norm and  $\tau = 6$  months. The initial and final perturbation SST are shown in (a) and (b), and the initial and final ABL perturbation  $\theta$  are shown in (c) and (d). The growth factor  $\mu$  of  $\mathcal{T}'$  is indicated. Shaded and unshaded regions indicate perturbations of opposite sign. The contour interval and is arbitrary.

$$+ \underbrace{2 \int_0^t \int_V \frac{T}{a^2} \left( \frac{1}{\cos^2 \varphi} \frac{\partial}{\partial \lambda} \left( A_H \frac{\partial T}{\partial \lambda} \right) + \frac{\partial}{\partial \varphi} \left( A_H \frac{\partial T}{\partial \varphi} \right) \right) + \frac{\partial}{\partial z} \left( A_V T \frac{\partial T}{\partial z} \right)}_D dV dt \quad (5)$$

where  $\bar{\mathbf{U}} = \bar{U}\mathbf{i} + \bar{V}\mathbf{j} + \bar{W}\mathbf{k}$  and  $\bar{T}$  represent the basic state ocean velocity and temperature field components of  $\mathbf{S}_0$  in (1);  $\mathbf{u} = u\mathbf{i} + v\mathbf{j} + w\mathbf{k}$  and  $T$  are the perturbation ocean velocity and temperature components of  $\mathbf{s}$ ;  $A_H$  and  $A_V$  are the horizontal and vertical coefficients of eddy diffusivity; and  $dV = a \cos \varphi d\lambda d\varphi dz$  is a volume element. Terms A, B and C represent the contribution to  $\mathcal{T}$  of perturbation horizontal and vertical heat fluxes, while term D represents dissipation processes and surface sources and sinks. The amplitude of each perturbation was normalised so that  $\mathcal{T}(0) = 1$ .

The time history of each term in (5) for OP1 of Model 1 is shown in Figure 11a, and provides a direct measure of the contribution of each term in (5) to the growth factor  $\mu$  of  $\mathcal{T}$ . Figure 11a indicates that all terms in (5) contribute significantly to the growth of OP1 in Model 1, although further analysis reveals that point-by-point the integrand of terms B and C almost balance. Thus the major contributor to the growth of  $\mathcal{T}$  is term A which represents the influence of perturbation zonal heat fluxes on  $\mathcal{T}$ . Figure 11b shows a vertical section of  $\mathcal{F} = -\frac{uT}{a \cos \varphi} \partial \bar{T} / \partial \lambda - \frac{vT}{a} \partial \bar{T} / \partial \varphi - wT \partial \bar{T} / \partial z$  along the equator at time 3 months, and indicates largest growth for Model 1 occurs primarily above and within the thermocline in the eastern Pacific. It is in the eastern Pacific that the model response to OP1 is largest as shown in Figs. 8b and 9b. The SST perturbations that develop in the east produce wind stress anomalies are like those shown in Fig. 4b as the most unstable eigenmode emerges. These wind stress anomalies drive changes in the zonal velocity and Ekman transport in the upper ocean. The associated changes in Ekman-induced  $w$  are primarily balanced by changes in  $v$ , while changes in  $u$  yield rapid growth of  $\mathcal{T}$  in the thermocline since  $\frac{1}{a \cos \varphi} \partial \bar{T} / \partial \lambda$  is relatively large in the east Pacific.

The contribution of each term in (5) to the growth of OP1 for Model 2 is shown in Figure 11c. In this case term C accounts for all of the growth of  $\mathcal{T}$  for the optimal perturbation. A vertical section of  $\mathcal{F}$  along the equator is shown in Fig. 11d and is largest in the upper thermocline of the west Pacific. As the most unstable eigenmode emerges, the corresponding wind stress perturbations (Fig. 4d) drive perturbation Ekman-induced  $w$ . These are largest in the west Pacific in the upper thermocline where  $\partial \bar{T} / \partial z$  is relatively large also.

The picture for the fastest growing optimal perturbation of Model 3 for the  $\mathcal{T}$  norm is qualitatively very similar to that for Model 2 (not shown). Instead we consider the growth of the optimal perturbation of Model 3 for the  $\mathcal{T}'$  norm. The contribution of the ABL to  $\mathcal{T}'$  is derived from the tangent linear form of the equation for boundary layer potential temperature (equation (6) of Kleeman and Power (1995)). Contributions to  $\mathcal{T}'$  from the ABL arise from surface heat exchange between the ocean and ABL (denoted SHE), advection through the top of the ABL (denoted VADV), and dissipative processes (denoted DISS). The time history of SHE, VADV, DISS and each term in (5) is shown in Fig. 11ef for OP1 of the  $\mathcal{T}'$  norm of Model 3. As in the preceding cases, a significant component of the growth of  $\mathcal{T}'$  is due to term C in (5), but now is augmented by the surface exchange of heat between the ABL and ocean. The growth of SHE is largely offset by DISS.

### 4.3 The Energy Norm

The second norm considered was the basin-integrated ocean perturbation energy denoted  $E$  given by:

$$E = \frac{\rho_o}{2} \int_{-H(\lambda, \varphi)}^0 \int_{\lambda_w}^{\lambda_e} \int_{\varphi_s}^{\varphi_n} (u^2 + v^2 + (g\rho/\rho_o \bar{N})^2) a \cos \varphi d\lambda d\varphi dz \quad (6)$$

where  $\rho$  is the perturbation density,  $\bar{N}(\lambda, \varphi, z)$  is the Brunt-Väisälä frequency of the basic state  $\mathbf{S}_0$ , and  $g$  is the

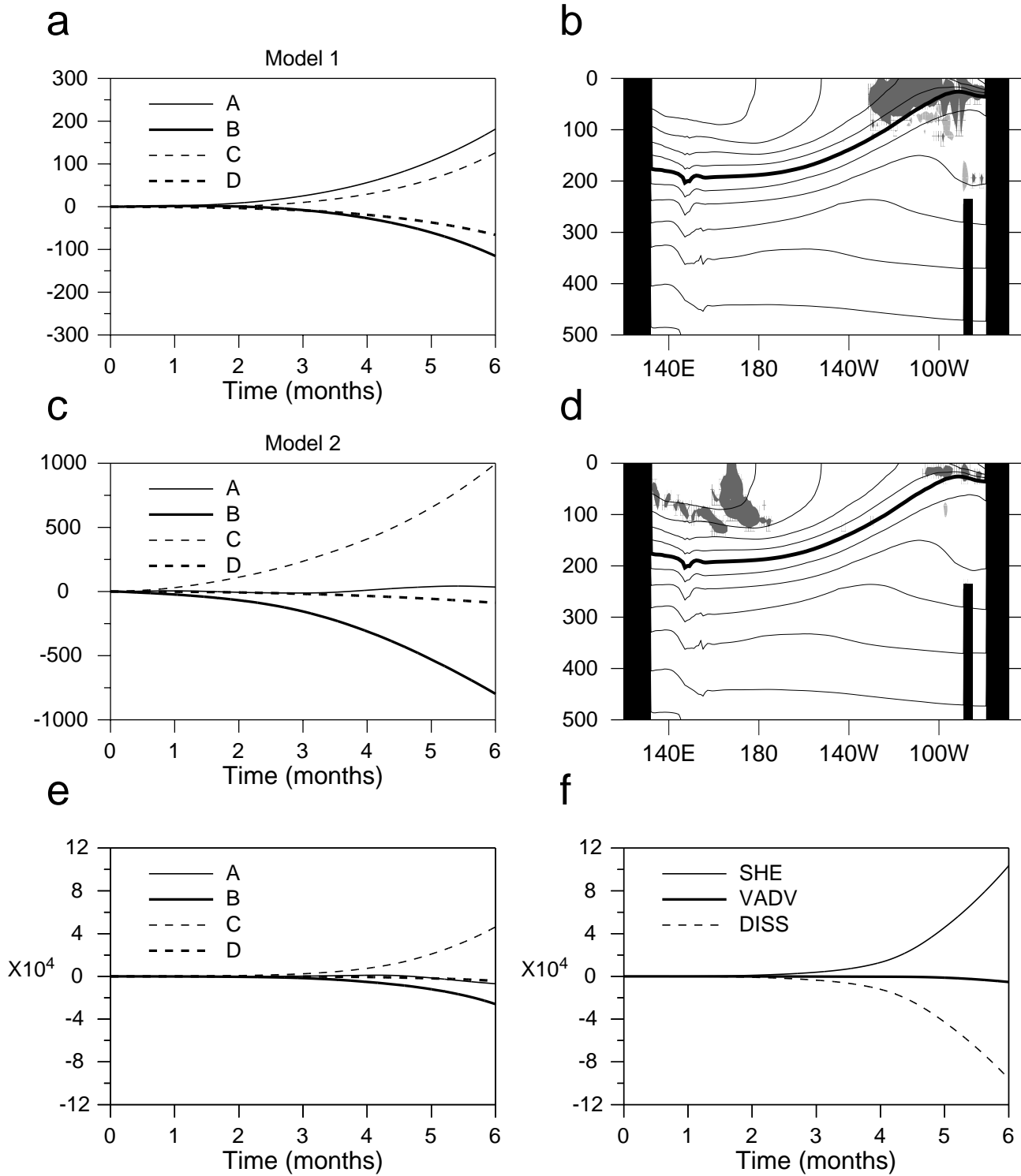


Figure 11: Timeseries of Term A, Term B, Term C, and Term D in equation (5) for the fastest growing optimal perturbation of (a) Model 1, and (c) Model 2 using the  $\mathcal{T}$  norm for  $\tau = 6$  months. A vertical section of  $-\frac{uT}{a\cos\phi}\partial\bar{T}/\partial\lambda - \frac{vT}{a}\partial\bar{T}/\partial\phi - wT\partial\bar{T}/\partial z$  along the equator at 3 months is shown in (b) for Model 1, and (d) for Model 2. Dark (light) shading indicates areas of heating (cooling). The contours denote the basic state temperature  $\bar{T}$  with a  $2^\circ\text{C}$  contour interval. The bold contour is the  $20^\circ\text{C}$  isotherm. Timeseries of SHE, VADV, DISS and each term in equation (5) for the fastest optimal perturbation of Model 3 using the  $\mathcal{T}'$  norm for  $\tau = 6$  months are shown in (e) and (f).

acceleration due to gravity. For simplicity, the linear equation of state  $\rho = \rho_o(\alpha T + \beta S)$  was used to derive (6) where  $\alpha = -2.489 \times 10^{-4} \text{ kg m}^{-3} \text{ K}^{-1}$  and  $\beta = 7.453 \times 10^{-4} \text{ kg m}^{-3} \text{ psu}^{-1}$  are the expansion coefficients for temperature and salinity respectively, and  $\rho_o = 1020 \text{ kg m}^{-3}$ . This norm is of obvious interest since it indicates how perturbation energy can be exchanged with the basic state flow via barotropic and baroclinic processes. In Model 3,  $\theta = 0$  at initial time since  $\theta$  does not contribute to  $E$ . For  $E$  the matrix  $\mathbf{X}$  of section 3.2 is singular and cannot be factorized. However, this problem may be circumvented if  $S = 0$  at initial time.

The SST and upper ocean temperature along the equator of OP1 for Model 1 using the  $E$  norm is shown in Figs. 12ab and 13ab. At the surface, the initial structure of OP1 for the  $E$  norm is confined to the far eastern tropical Pacific (Fig. 12a) and follows the thermocline at depth (Fig. 13a). Like the  $\mathcal{T}$  optimal, the  $E$  optimal evolves into the most unstable eigenmode (cf Fig. 3b).

OP1 of Model 2 using the  $E$  norm is shown in Figs. 12cd and Figs. 13cd. A comparison of Fig. 12c with Fig. 8c reveals a number of similarities between the initial SST structures of the  $E$  and  $\mathcal{T}$  optimals in the western Pacific. Like the  $\mathcal{T}$  optimal, the  $E$  optimal evolves into the most unstable eigenmode of Model 2 (see Fig. 3d). Figure 13c reveals a subsurface dipole in the vertical in the far western Pacific centered around 75m depth.

The surface signature of the fastest growing  $E$  optimal of Model 3 is similar to that of the  $\mathcal{T}$  optimal as shown in Fig. 12e. The subsurface structure is similar to that of Model 2 (Fig. 13e) and like the other optimal perturbations it evolves into the most unstable eigenmode. The growth factor  $\mu = 15568$ , is some 50 times larger than that of Models 1 and 2. We will comment further on these large growth factors in section 5.

Differences in the structure of the optimal perturbations of the  $\mathcal{T}$  and  $E$  norms are to be expected based on section 3.2. The adjoint eigenmodes described there are defined with respect to an inner-product that defines the L2-norm of the coupled system. If an energy norm could be used to define the adjoint operator, one phase of the adjoint eigenmodes of that operator would resemble the optimal perturbations of the  $E$  norm presented here. However as noted above the use of such a norm to define the adjoint is problematic since the matrix  $\mathbf{X}$  discussed in section 3.2 is singular and cannot be factorized.

#### 4.4 Dynamics of $E$ Optimals

The time evolution of  $E$  is given by:

$$\begin{aligned}
 E(t) = E(0) & - \underbrace{\rho_o \int_0^t \int_V \frac{u}{a \cos \varphi} \left( u \frac{\partial \bar{U}}{\partial \lambda} + v \frac{\partial \bar{V}}{\partial \lambda} \right) + \frac{v}{a} \left( u \frac{\partial \bar{U}}{\partial \varphi} + v \frac{\partial \bar{V}}{\partial \varphi} \right) + w \left( u \frac{\partial \bar{U}}{\partial z} + v \frac{\partial \bar{V}}{\partial z} \right) dV dt}_A \\
 & - \underbrace{\rho_o \int_0^t \int_V \rho \left( \frac{g}{\rho_o \bar{N}} \right)^2 \left[ \frac{u}{a \cos \varphi} \frac{\partial \bar{\rho}}{\partial \lambda} + \frac{v}{a} \frac{\partial \bar{\rho}}{\partial \varphi} \right] dV dt}_B \\
 & + \underbrace{\rho_o \int_0^t \int_V (u \nabla \cdot (A_{mH} \nabla u) + v \nabla \cdot (A_{mH} \nabla v)) + \left( u \frac{\partial}{\partial z} \left( A_{mV} \frac{\partial u}{\partial z} \right) + v \frac{\partial}{\partial z} \left( A_{mV} \frac{\partial v}{\partial z} \right) \right)}_{C1} \\
 & + \underbrace{\rho \left( \frac{g}{\rho_o \bar{N}} \right)^2 \left( \nabla \cdot (A_H \nabla \rho) + \frac{\partial}{\partial z} \left( A_V \frac{\partial \rho}{\partial z} \right) \right)}_{C2} dV dt
 \end{aligned} \tag{7}$$

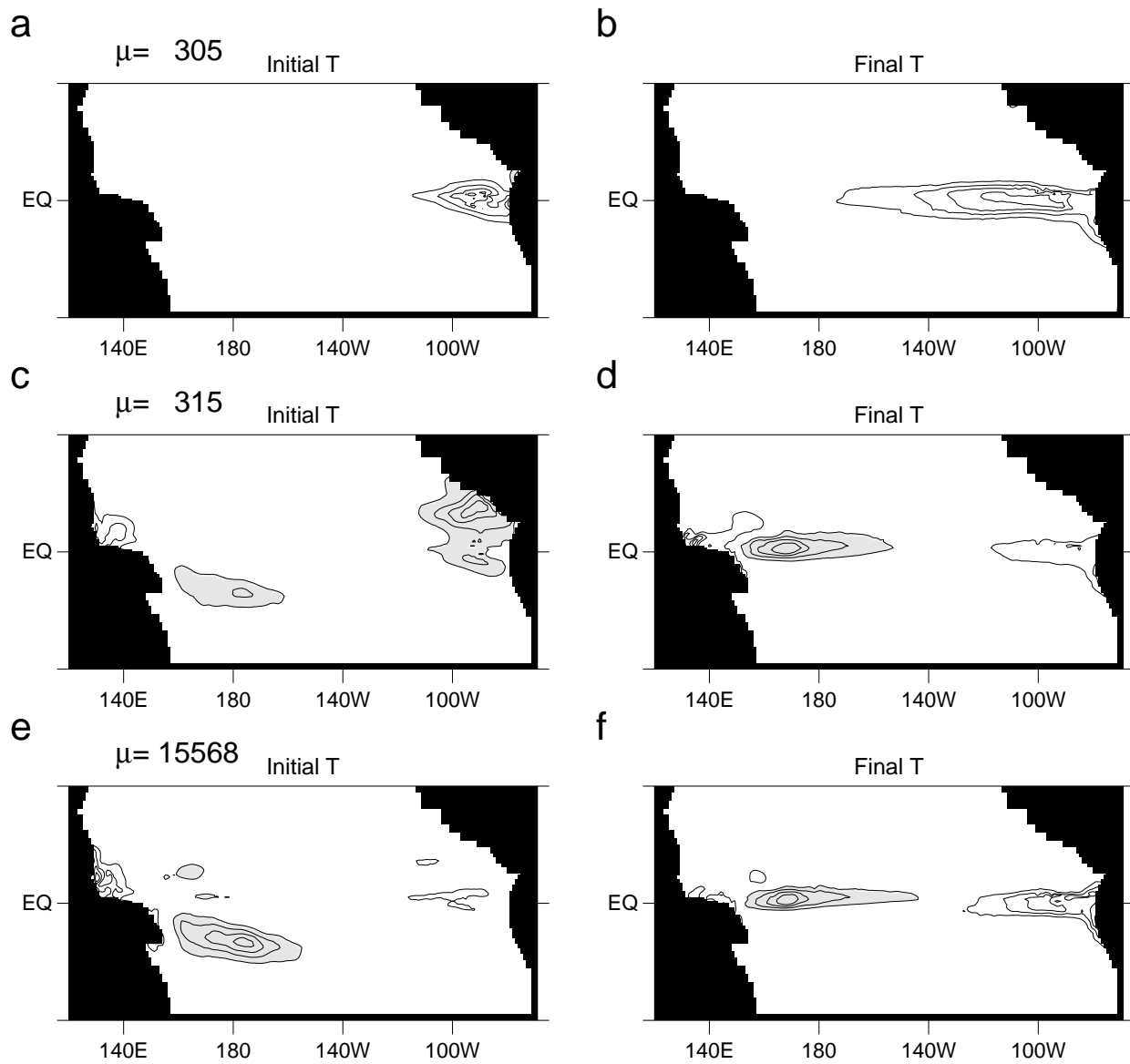


Figure 12: Same as Fig. 8 but for the fastest growing optimal perturbation of the  $E$  norm. (e) and (f) show OP1 for Model 3.

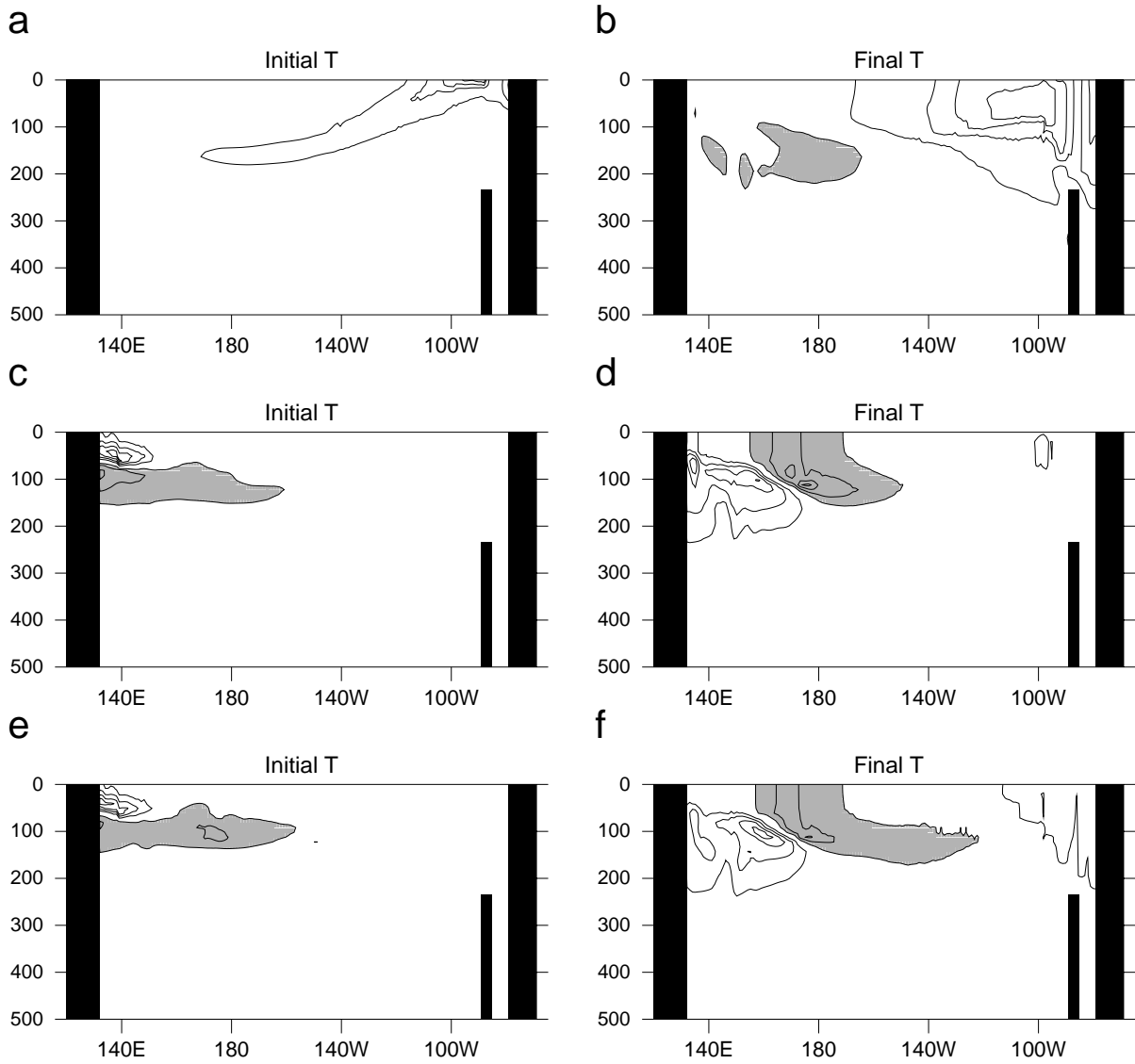


Figure 13: Same as Fig. 9 but for the fastest growing optimal perturbation of the  $E$  norm. (e) and (f) show OP1 for Model 3.

where  $A_{mH}$  and  $A_{mV}$  are the horizontal and vertical eddy viscosities respectively, and  $\bar{\rho}$  is the basic state density. Terms A and B represent the release of perturbation energy from the basic state due to barotropic and baroclinic processes respectively, and terms (C1+C2) collectively represent net sources and sinks at the surface due to surface fluxes and dissipation. Each OP is normalized so that  $E(0) = 1$ .

Figure 14 shows the time evolution of each term in (7) for OP1 of the  $E$  norm for Models 1 and 2. Model 3 is very similar to Model 2, apart from the larger  $E$  growth factor, and is not shown. In all cases the growth of  $E$  is dominated by baroclinic processes as described by term B. A vertical section of the integrand of term B is also shown in Fig. 14 after 3 months for each perturbation. In Model 1, Fig. 14b shows that the east Pacific is favoured for the growth of  $E$  where the equatorial undercurrent approaches the surface. To understand this, it is useful to remember that the growth of perturbations by baroclinic processes is a form of thermal convection (Pedlosky, 1979). For this to occur horizontal gradients of potential density are required. At middle latitudes these gradients can be maintained by the Coriolis force as described by the thermal wind relation. At the equator in the Pacific Ocean where  $f = 0$  the zonal density and pressure gradients are maintained by the easterly surface trade winds. The region where the undercurrent rises to the surface in the east Pacific is also a region of large horizontal temperature and density gradients (cf Fig. 2b) since the undercurrent itself is driven by the zonal pressure gradient below the surface within the thermocline (Gill, 1982). Thus the necessary conditions for baroclinic energy release are present in this region.

In Models 2 and 3 (Fig. 14d), the western Pacific is favoured for growth of  $E$  in regions where the basic state stratification is weak since it is here that thermal convection can occur most readily. In these regions  $1/\bar{N}^2$  in (7) will be very large. A comparison of Figs. 11bd and 14bd reveals that the geographic locations of maximum growth of  $\mathcal{T}$  and  $E$  largely coincide, indicating that the same regions of the ocean are susceptible to non-normal perturbation growth irrespective of the choice of perturbation growth norm.

## 5 Summary and Conclusions

We have explored the properties and dynamics of the optimal perturbations of a hierarchy of hybrid coupled ocean-atmosphere models of the tropical Pacific. The coupled model hierarchy was constructed so as to yield information about the dependence of optimal perturbation structure and growth rate on atmospheric dynamics and air-sea interaction processes. Each hybrid coupled model shares the same OGCM while three different atmospheric models of varying complexity were employed. These same three atmospheric models have also been coupled to a  $1\frac{1}{2}$ -layer ocean model, and the resulting intermediate coupled models employed in a series of studies by some of the authors to explore the optimal perturbations of ENSO (Moore and Kleeman, 1996; 1997ab). The commonality of the atmospheric models employed in these two sets of models means that a direct comparison of the results is possible and meaningful. The optimal perturbation studies using the aforementioned intermediate coupled models, and others cited in section 1, have revealed the following:

- (1) The optimal perturbation spectrum is typically dominated by one member;
- (2) The dominant optimal perturbation evolves into the gravest coupled ocean-atmosphere eigenmode of the system;
- (3) The optimal perturbations of coupled models that utilize statistical models of the atmosphere emphasize the sensitivity of the central and east Pacific to perturbation growth;
- (4) The optimal perturbations of coupled models that include a parameterization for deep atmospheric convection emphasize the sensitivity of the west Pacific warm pool to perturbation growth;

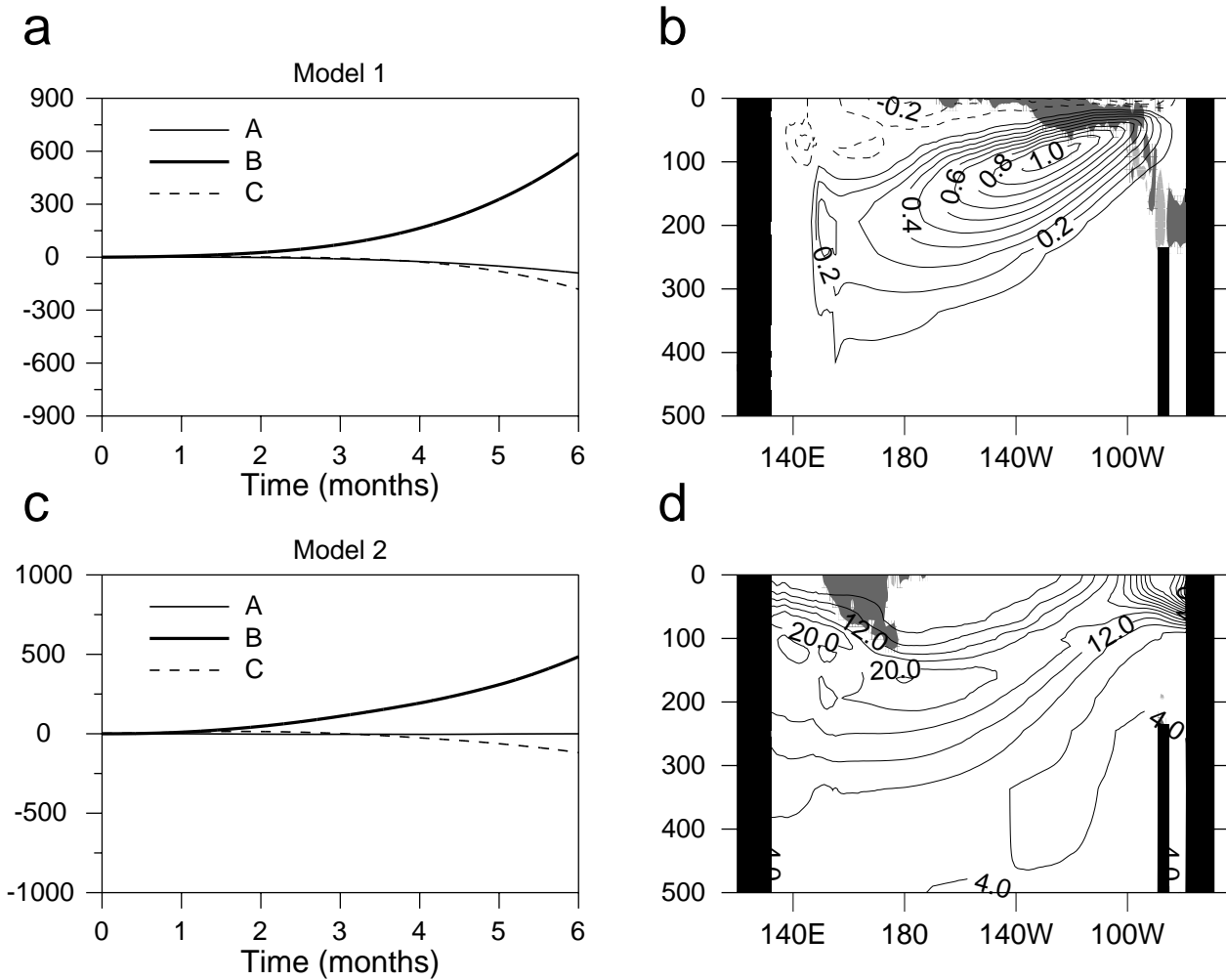


Figure 14: Timeseries of Term A, Term B, and Term C=C1+C2 in equation (7) for the fastest growing optimal perturbation of (a) Model 1, and (c) Model 2 using the  $\mathcal{T}$  norm for  $\tau = 6$  months. A vertical section of  $\rho_o(g/\rho_o\bar{N})^2\rho(u\partial\bar{p}/\partial x + v\partial\bar{p}/\partial y)$  along the equator at 3 months is shown in (b) for Model 1, and (d) for Model 2. Dark (light) shading indicates areas where potential energy is liberated from (given to) the basic state. In (b) the contours are the basic state zonal velocity  $\bar{U}$  with a  $0.1 \text{ m s}^{-1}$  contour interval. Westward flows are indicated by dashed contours. In (d) the contours are the basic state Brunt-Väisälä frequency  $\bar{N}^2$ , and the contour interval is  $4 \times 10^{-5} \text{ s}^{-2}$ .

- (5) The degree of non-normality of the gravest coupled ocean-atmosphere eigenmode is strongly controlled by the atmospheric component of the coupled system;
- (6) The structure of the optimal perturbations for models with a dynamical atmosphere are relatively insensitive to the choice of perturbation growth norm.

The results of previous studies of the optimal perturbations for ENSO using intermediate coupled models are therefore supported by the hybrid coupled models used here and appear to be robust. With regard to (6), the optimal perturbations of Models 1 and 2 do show some sensitivity to the choice of norm. However, the geographical location of maximum growth is the same for both norms considered.

In general, the growth factors of the optimal perturbations of the hybrid coupled models considered here are higher than those found in intermediate coupled models. Further investigation has revealed that the hybrid model growth factors are probably an over estimate of what may be achieved by the same perturbations in the non-linear model. This is associated with the limitations of the tangent linear approximation in each coupled model. The primary factor limiting the validity of the tangent linear assumption appears to be the turbulent kinetic energy (TKE) vertical mixing scheme of Blanke and Delecluse (1993) employed in the OGCM. A simplified version of this scheme was used by necessity in the tangent linear model and adjoint model following the practice of numerical weather prediction (Mahfouf, 1999). Depending on perturbation amplitude and structure, perturbations in the non-linear model may degenerate quickly into large amplitude, small scale disturbances as the TKE mixing scheme attempts to remove vertical density gradients in the upper ocean where the stratification is already weak (see Fig. 14d). This type of behaviour has important implications for the computation of optimal perturbations that can be used for generating forecast ensembles, especially when considering the optimal perturbations of time evolving basic states in areas where the TKE mixing is very active. In addition, the presence of large local density or velocity gradients in the basic state can yield rapidly growing optimal perturbations that violate the tangent linear assumption on seasonal timescales. In this paper these problems were largely circumvented by considering the optimal perturbations of a time averaged circulation. However, these important aspects of the system are currently under further investigation and will be the subject of a future publication.

Nonetheless, allowing for limitations of the tangent linear assumption, the higher growth factors of the optimal perturbations presented here are consistent with those of some intermediate coupled models. For example, Moore and Kleeman (1997b) found that as the complexity of the ocean component of an intermediate model was increased by adding perturbation horizontal and vertical advection, the growth factors of the optimal perturbations also increased.

In conclusion, the results of previous studies using intermediate coupled models, and the results of the present study suggest that the structure of the optimal perturbations of low-frequency tropical coupled ocean-atmosphere modes such as ENSO is influenced more by atmospheric dynamics and the details of the air-sea interactions processes than by ocean dynamics. In addition, the hybrid coupled models used here suggest a number of potentially important perturbation growth mechanisms that may influence the growth of disturbances in CGCMs and limit the predictability of ENSO. Using hybrid coupled models to compute optimal perturbations for generating CGCM ensemble forecasts may therefore be one way of circumventing the challenging problem of computing such perturbations directly using a CGCM. The ability of CGCMs to support perturbation growth via the mechanisms suggested by the hybrid coupled models is currently under investigation.

## Acknowledgements

AMM was supported by a research grant from the NSF Division of Climate (ATM-9809790). We are indebted to Dan Sorensen for making ARPACK so freely available.

## Appendix

### Optimal Perturbations: An Illustrative Example

For readers not familiar with all of the ideas discussed in this paper, it is very instructive and illuminating to consider a simple system as an illustrative example. The system we shall consider is a variant of the system considered by Farrell and Ioannou (1996). Consider the autonomous linear system described by:

$$\frac{\partial \mathbf{s}}{\partial t} = \mathbf{A} \mathbf{s} \quad (\text{A1})$$

where  $\mathbf{s}$  represents a 2-dimensional state vector, and:

$$\mathbf{A} = \begin{pmatrix} \sigma_1 & (\sigma_2 - \sigma_1) \cot \delta \\ 0 & \sigma_2 \end{pmatrix}. \quad (\text{A2})$$

The parameters  $\sigma_1$ ,  $\sigma_2$  and  $\delta$  are real and  $0 \leq \delta \leq \pi$ . Eigensolutions of (A1) will be denoted  $\mathbf{s}_1(t) = a_1 \hat{\mathbf{s}}_1 e^{\sigma_1 t}$  and  $\mathbf{s}_2(t) = a_2 \hat{\mathbf{s}}_2 e^{\sigma_2 t}$ , where  $\hat{\mathbf{s}}_1^T = (1, 0)$  and  $\hat{\mathbf{s}}_2^T = (\cos \delta, \sin \delta)$  are the unit eigenvectors of (A2) (superscript  $T$  denotes the transpose), with eigenvalues  $\sigma_1$  and  $\sigma_2$ , and  $a_1$  and  $a_2$  are the initial eigenmode amplitudes.

Solutions of (A1) are  $\mathbf{s}(t) = \mathbf{R}(t) \mathbf{s}(0)$ , where  $\mathbf{R}(t) = e^{\mathbf{A}t}$  is the propagator. The norm  $\mathcal{N}(t) = \mathbf{s}^T(t) \mathbf{s}(t)$  will be used as a measure of perturbation amplitude, and the perturbation that produces the maximum value of the growth factor  $\mu_{\mathcal{N}} = \mathcal{N}(\tau) / \mathcal{N}(0)$  during the time interval  $\tau$  is the right singular vector of  $\mathbf{R}(\tau)$  with largest singular value (Noble and Daniel, 1988). This perturbation is also referred to as the optimal perturbation, and  $\tau$  as the optimal growth time. As an example, Fig. A1a shows  $\mu_{\mathcal{N}}(\tau)$  vs  $\tau$ , for the optimal perturbation of (A1) where  $\delta = 4\pi/5$ ,  $\sigma_1 = -0.05$  and  $\sigma_2 = -0.5$ , and reveals that for a range of  $\tau$  perturbation growth is possible ( $\mu_{\mathcal{N}} > 1$ ) even though both  $\mathbf{s}_1$  and  $\mathbf{s}_2$  decay in time.

A specific case is illustrated in Figs. A1b-e when  $\tau = 4$ , which is the case for which  $\mathcal{N}$  achieves its largest value in Fig. A1a for the current choice of  $\delta$ ,  $\sigma_1$  and  $\sigma_2$ . Figures A1b-e show the time evolution of the optimal perturbation, denoted OP, and its projection on the eigenmodes  $\mathbf{s}_1$  and  $\mathbf{s}_2$ . At time  $t = 0$ , OP has  $\mathcal{N}(0) = 1$ . Figures A1c-e show that the rapid decay of  $\mathbf{s}_2$  compared to  $\mathbf{s}_1$  causes OP to rotate in the direction of  $\mathbf{s}_1$  and grow in amplitude during the interval  $t \in [0, 4]$ . For  $t > 4$  OP decays in amplitude.

The growth factor  $\mu_{\mathcal{N}}$  of OP depends on the eigenvalues  $\sigma_1$ ,  $\sigma_2$ , and on the angle  $\delta$  between the eigenmodes. This dependence is illustrated in Figures A2ab which show contours of  $\log_{10}(\mu)$  for  $\sigma_1$  vs  $\delta$  and  $\sigma_2/\sigma_1$  vs  $\delta$  for particular parameter combinations. A wide range of situations are captured by Figs. A2ab corresponding to different combinations of growing and decaying eigenmodes  $\mathbf{s}_1$  and  $\mathbf{s}_2$ . The angle  $\delta$  is a direct measure of the linear dependence of the eigenmodes (see Fig. A1b). When  $\delta = \pi/2$ ,  $\mathbf{A}$  is a normal matrix and  $\hat{\mathbf{s}}_1$  and  $\hat{\mathbf{s}}_2$  are linearly independent and orthogonal. In this case no perturbations can grow faster than the most unstable eigenmode of the system, and if  $\sigma_1 < 0$  and  $\sigma_2 < 0$  all perturbations must decay in time as confirmed by Fig. A2a. For  $\delta \neq \pi/2$ ,  $\mathbf{A}$  is a non-normal matrix and its eigenmodes are linearly dependent. As  $\delta \rightarrow 0$  or  $\delta \rightarrow \pi$  large transient perturbation growth is possible and Figs. A2ab indicate that  $\mu_{\mathcal{N}} \rightarrow \infty$  even when both eigenmodes decay in time. When at least one of the eigenmodes is unstable, Fig. A2ab shows that the OP grows much more rapidly than the exponential growth anticipated for the most unstable eigenmode.

Due to the large computational cost, it is possible to compute only the most unstable member of the eigenspectra for the complex coupled models described in the main text. Therefore, it will not be possible to compute the

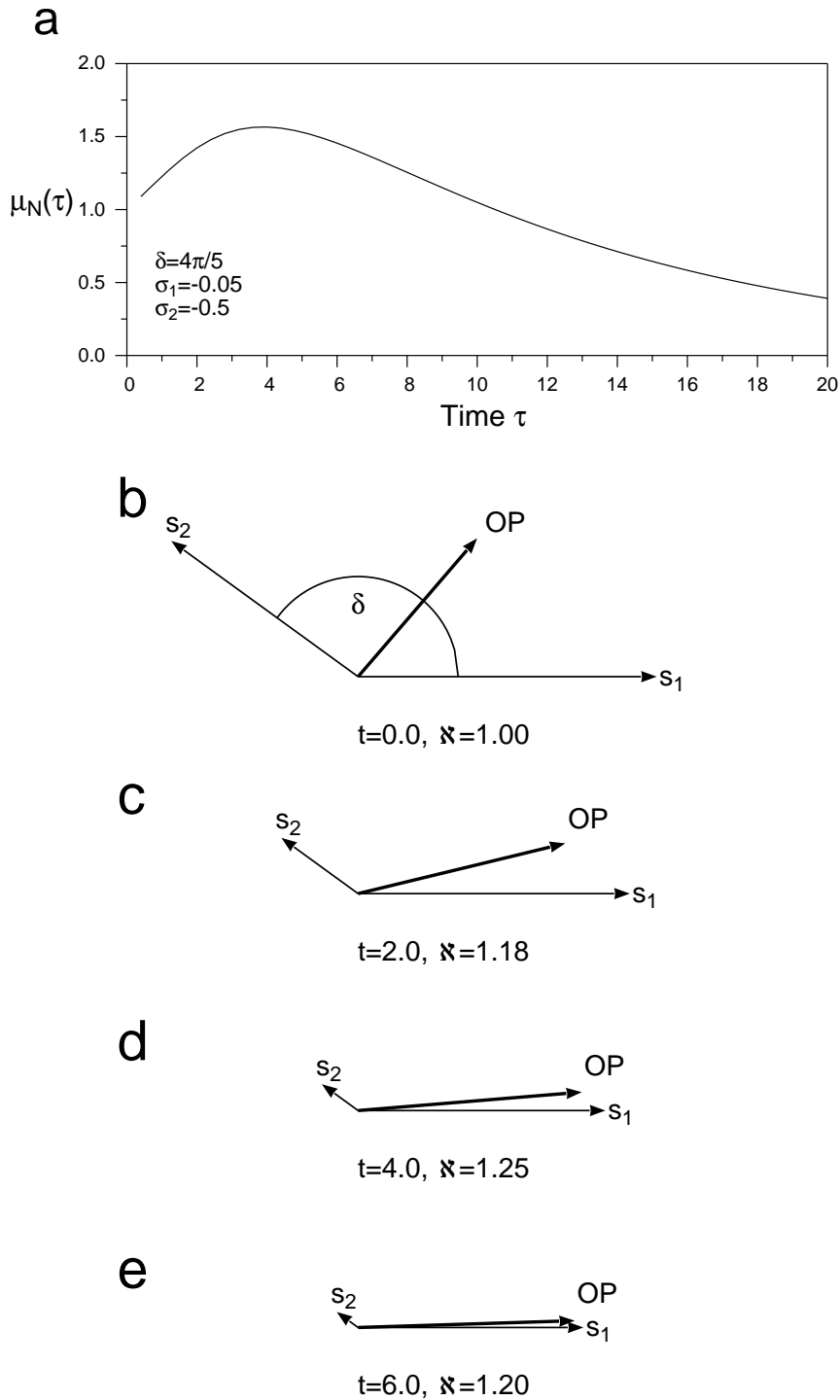


Figure 1: A1: (a) The growth factor  $\mu$  vs  $\tau$  of the fastest growing optimal perturbation of the  $2 \times 2$  system described by equations (A1) and (A2) for the parameter choice indicated. (b-e) The relative orientation of OP,  $s_1$  and  $s_2$  as a function of time  $t$  for  $\delta = 4\pi/5$ ,  $\sigma_1 = -0.05$ ,  $\sigma_2 = -0.5$  and  $\tau = 4$ . In each case the size of the L2-norm  $\mathfrak{N}$  is indicated.

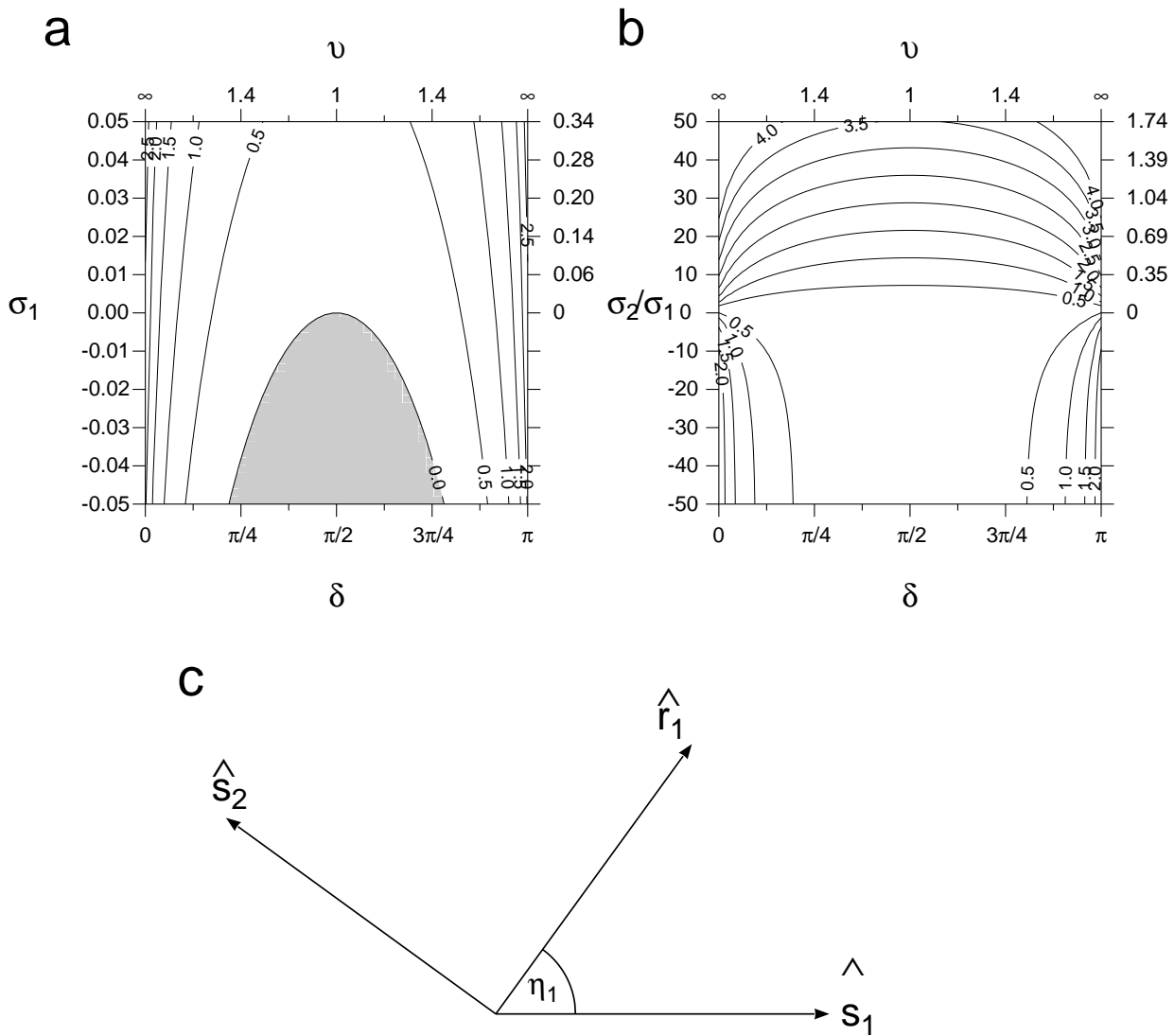


Figure 2: A2: (a) A contour plot of  $\log_{10}(\mu)$  for  $\sigma_1$  vs  $\delta$  for the case  $\sigma_2 = -0.5$  and  $\tau = 8$ . The numbers on the right hand ordinate represent  $\log_{10}$  of the growth factor of the L2-norm for a perturbation with the structure of the most unstable eigenmode when  $\sigma_1 > 0$ . (b) Same as (a) except for  $\sigma_2/\sigma_1$  vs  $\delta$  for  $\sigma_1 = 0.01$  and  $\tau = 8$ . Shading indicates  $\mu < 1$  and  $\nu_1 = 1/\cos(\delta - \pi/2)$ . (c) A schematic showing the relative orientation of the eigenmodes of equations (A1) and (A2) and the adjoint eigenmode  $\hat{r}_1$ .

angles  $\delta$  directly. However, an alternative measure of the degree of non-normality of  $\mathbf{A}$  can be computed following Farrell and Ioannou (1999) that makes direct use of the biorthogonality relation between the eigenvectors of  $\mathbf{A}$  and of  $\mathbf{A}^T$ , namely:

$$\hat{\mathbf{s}}_n^T \hat{\mathbf{r}}_m (\sigma_n - \sigma_m) = 0 \quad (\text{A3})$$

where  $\hat{\mathbf{r}}_m$  are the eigenvectors of  $\mathbf{A}^T$ , often referred to as the adjoint eigenmodes. For the system considered here,  $\hat{\mathbf{r}}_1$  is orthogonal to  $\hat{\mathbf{s}}_2$  and  $\hat{\mathbf{r}}_2$  is orthogonal to  $\hat{\mathbf{s}}_1$ .

Consider now:

$$v_n = \frac{|\hat{\mathbf{r}}_n| |\hat{\mathbf{s}}_n|}{\hat{\mathbf{r}}_n^T \hat{\mathbf{s}}_n} = \frac{1}{\cos \eta_n} \quad (\text{A4})$$

where  $\eta_n$  is the angle subtended by  $\hat{\mathbf{s}}_n$  and  $\hat{\mathbf{r}}_n$ . For the case considered here,  $\hat{\mathbf{r}}_1^T = (\sin \delta, -\cos \delta)$  and  $\hat{\mathbf{r}}_2 = (0, 1)$ . The relative orientation of  $\hat{\mathbf{r}}_1$  and  $\hat{\mathbf{s}}_1$  is illustrated in Fig. A2c where clearly  $\eta_1 = \delta - \pi/2$ . Figure A2c indicates that as  $\delta \rightarrow \pi$  or  $\delta \rightarrow 0$ , the angle  $\eta_1 \rightarrow \pm\pi/2$ , in which case  $v_1 \rightarrow \infty$ . Thus a large value of  $v_1$  is indicative of a highly non-normal system. This idea is illustrated in Fig. A2ab where  $\log_{10}(\mu)$  is also shown as a function of  $\sigma_1$  vs  $v_1$  and  $\sigma_2/\sigma_1$  vs  $v_1$ .  $v_n$  is a useful measure of the degree of non-normality of each eigenmode of systems more complicated than that considered here, and can be readily obtained when only a handful of eigenmodes and their corresponding adjoint eigenmodes can be computed.

Figures A2ab reveal that optimal perturbation growth ( $\log_{10}(\mu) > 0$ ) is possible for a wide range of parameters, and that the same growth factor can be obtained for a range of parameter values. For the coupled models considered in this study, the eigenmodes are complex so in addition to exponential growth and decay they also oscillate in time. The oscillation frequency of the eigenmodes will also influence the optimal perturbation growth factors.

## References

- Balmaseda, M.A., Davey, M.K. and D.L.T. Anderson, 1995: Decadal and seasonal dependence of ENSO predictive skill. *J. Climate*, **8**, 2705-2715.
- Barkmeijer, J., Van Gijzen, M., and F. Bouttier, 1998: Singular vectors and estimates of the analysis-error covariance metric. *Q. J. Roy. Meteor. Soc.*, **124**, 1695-1713.
- Blanke, B. and P. Delecluse, 1993: Variability of the tropical Atlantic ocean simulated by a general circulation model with two different mixed layer physics. *J. Phys. Oceanogr.*, **23**, 1363-1388.
- Blumenthal, M.B., 1991: Predictability of a coupled ocean-atmosphere model. *J. Climate*, **4**, 766-784.
- Bretherton, C.S., C. Smith and J.M. Wallace, 1992: An intercomparison of methods for finding coupled patterns in climate data. *J. Climate*, **5**, 541-560.
- Buizza, R. and T.N. Palmer, 1995: The singular-vector structure of the atmospheric global circulation. *J. Atmos. Sci.*, **52**, 1434-1456.

- Chen, Y.-Q., D.S. Battisti, T.N. Palmer, J. Barsugli and E.S. Sarachik, 1997: A study of the predictability of tropical Pacific SST in a coupled atmosphere/ocean model using singular vector analysis: The Role of the annual cycle and the ENSO cycle. *Mon. Wea. Rev.*, **125**, 831-845.
- Courant, R. and D. Hilbert, 1953: *Methods of Mathematical Physics*. Wiley Interscience.
- Eckert, C., 1999: On predictability limits of ENSO. A study performed with a simplified model of the tropical Pacific ocean-atmosphere system. Examensarbeit Nr. 55. Available from: Max Planck Institut fuer Meteorologie, Bundesstrasse 55 D-20146, Hamburg, Germany. 76pp.
- Fan, Y., M.R. Allen, D.L.T. Anderson and M.A. Balmaseda, 2000: How predictability depends on the nature of uncertainty in initial conditions in a coupled model of ENSO. *J. Climate*, **13**, 3298-3313.
- Farrell, B.F., 1982: The initial growth of disturbances in baroclinic flow. *J. Atmos. Sci.*, **39**, 1663-1686.
- Farrell, B.F., 1984: Modal and nonmodal baroclinic waves. *J. Atmos. Sci.*, **41**, 668-673.
- Farrell, B.F., 1985: Transient growth of damped baroclinic waves. *J. Atmos. Sci.*, **42**, 2718-2727.
- Farrell, B.F., 1988a: Optimal excitation of neutral Rossby waves. *J. Atmos. Sci.*, **45**, 163-172.
- Farrell, B.F., 1988b: Optimal excitation of perturbations in viscous shear flow. *Phys. Fluids*, **31**, 2093-2102.
- Farrell, B.F., 1989a: Optimal excitation of baroclinic waves. *J. Atmos. Sci.*, **46**, 1193-1206.
- Farrell, B.F., 1989b: Transient development in confluent and diffluent flow. *J. Atmos. Sci.*, **46**, 3279-3288.
- Farrell, B.F. and P.J. Ioannou, 1996: Generalized stability theory. Part I: Autonomous operators. *J. Atmos. Sci.*, **53**, 2025-2040.
- Farrell, B.F. and P.J. Ioannou, 1999: Perturbation growth and structure in time dependent flows. *J. Atmos. Sci.*, **56**, 3622-3639.
- Farrell, B.F., and A.M. Moore, 1992: An adjoint method for obtaining the most rapidly growing perturbation to oceanic flows. *J. Phys. Oceanogr.*, **22**, 338-349.
- Frederiksen, J.S., 1982: A unified three-dimensional instability theory for the onset of blocking and cyclogenesis. *J. Atmos. Sci.*, **39**, 969-982.
- Galanti, E., E. Tziperman, M. Harrison, A. Rosati, R. Giering and Z. Sirkes, 2001: The equatorial thermocline outcropping - A seasonal control on the tropical Pacific ocean-atmosphere instability strength. *J. Climate*, Submitted.
- Gill, A.E., 1980: Simple solutions for heat-induced tropical circulation. *Q. J. R. Meteorol. Soc.*, **106**, 447-462.
- Gill, A.E., 1982: *Atmosphere Ocean Dynamics*. Academic Press, pp662.
- Hartmann, D.L., R. Buizza and T.N. Palmer, 1995: Singular vectors: the effect of spatial scale on linear growth of disturbances. *J. Atmos. Sci.*, **52**, 3885-3894.
- Jin, F.-F. and J.D. Neelin, 1993a: Modes of interannual tropical ocean-atmosphere interaction - a unified view. Part I: Numerical results. *J. Atmos. Sci.*, **21**, 3477-3503.
- Jin, F.-F. and J.D. Neelin, 1993b: Modes of interannual tropical ocean-atmosphere interaction - a unified view. Part III: Analytical results in fully coupled cases. *J. Atmos. Sci.*, **21**, 3523-3540.

- Kleeman, R. 1989: A modelling study of the effect of the Andean mountains on the summertime circulation of tropical South America. *J. Atmos. Sci.*, **46**, 3344-3362.
- Kleeman, R., 1991: A simple model of the atmospheric response to ENSO sea surface temperature anomalies. *J. Atmos. Sci.*, **48**, 3-18.
- Kleeman, R., 1993: On the dependence of hindcast skill on ocean thermodynamics in a coupled ocean-atmosphere model. *J. Climate*, **6**, 2012-2033.
- Kleeman R., J.P. McCreary and B.A. Klinger, 1999: A mechanism for the decadal variation of ENSO. *Geophys. Res. Lett.*, **26**, 1743.
- Kleeman, R. and S.B. Power, 1995: A simple atmospheric model for the surface heat flux of the ocean. *J. Phys. Oceanogr.*, **25**, 92-105.
- Latif, M. and M. Flügel, 1991: An investigation of short range climate predictability in the tropical Pacific. *J. Geophys. Res.*, **96**, 2661-2673.
- Latif, M. and A. Villwock, 1990: Interannual variability in the tropical Pacific as simulated in coupled ocean-atmosphere models. *J. Mar. Systems*, **1**, 51-60.
- Lau, K.-M. and P.H. Chan, 1985: Aspects of the 40-50 day oscillation during the northern winter as inferred from outgoing longwave radiation. **113**, 1889-1909.
- Lau, K.-M. and P.H. Chan, 1986: The 40-50 day oscillation and the El Niño/Southern Oscillation: A new perspective. *Bull. Amer. Met. Soc.*, **67**, 533-534.
- Lau, K.-M. and P.H. Chan, 1988: Intraseasonal and interannual variations of tropical convection: A possible link between 40-50 day oscillation and ENSO? *J. Atmos. Sci.*, 506-521.
- Lehoucq, R.B., D.C. Sorensen and C. Yang, 1997: ARPACK users' guide: Solution of large scale eigenvalue problems with implicitly restarted Arnoldi methods. Rice University, 140pp.
- Levitus, S., 1982: Climatological atlas of the world ocean. NOAA Prof. Paper No. 13, U.S. Govt. Printing Office, 173pp.
- McPhaden, M.J., 1999: Genesis and evolution of the 1997-98 El Niño . *Science*, **283**, 950-954.
- Macías, J., D. Stephenson, L. Terray, M. Balmaseda and D.L.T. Anderson, 1996: ENSO and seasonal variability in a hybrid coupled model of the tropical Pacific. *Annales Geophysicae*, **14**, Part II. Oceans, Atmosphere, Hydrology and Nonlinear Geophysics. C647.
- Madec, G., P. Delecluse, M. Imbard and C. Levy, 1998: OPA 8.1 Ocean general circulation model reference manual. Institut Pierre Simon Laplace des Sciences l'Environnement Global, LODYC, Universite Pierre et Marie Curie, Paris.
- Mahfouf, J.-F., 1999: Influence of physical processes on the tangent-linear approximation. *Tellus*, **51A**, 147-166.
- Molteni, F., R. Mureau, and T.N. Palmer, 1993: Predictability and finite time instability of the northern winter circulation. *Quart. J. Roy. Meteor. Soc.*, **119**, 269-298.
- Moore, A.M., and B.F. Farrell, 1993: Rapid perturbation growth on spatially and temporally varying oceanic flows determined using an adjoint method: Application to the Gulf Stream. *J. Phys. Oceanogr.* **23**, 1682-1702.

- Moore, A.M. and R. Kleeman, 1996: The dynamics of error growth and predictability in a coupled model of ENSO. *Q. J. R. Meteorol. Soc.*, **122**, 1405-1446.
- Moore, A.M. and R. Kleeman, 1997a: The singular vectors of a coupled ocean-atmosphere model of ENSO. Part I: Thermodynamics, energetics and error growth. *Q. J. R. Meteorol. Soc.*, **123**, 953-981.
- Moore, A.M. and R. Kleeman, 1997b: The singular vectors of a coupled ocean-atmosphere model of ENSO. Part II: Sensitivity studies and dynamical significance. *Q. J. R. Meteorol. Soc.*, **123**, 983-1006.
- Moore, A.M. and R. Kleeman, 2001: The differences between the optimal perturbations of coupled models of ENSO. *J. Climate*, **14**, 138-163.
- Moore, A.M. and A.J. Mariano, 1999: The dynamics of error growth and predictability in a model of the Gulf Stream. Part I: Singular vector analysis. *J. Phys. Oceanogr.*, **29**, 158-176.
- Moore, A.M., Zavala-Garay, J. and C.L. Perez, 2001: A non-normal view of the ocean circulation. *J. Phys. Oceanogr.*, Submitted.
- Neelin, J.D. and F.-F. Jin, 1993: Modes of interannual tropical ocean-atmosphere interaction - a unified view. Part II: Analytical results in the weak coupling limit. *J. Atmos. Sci.*, **21**, 3504-3522.
- Noble, B. and J. Daniel, 1988: Applied Linear Algebra. Prentice Hall, 521pp.
- Palmer, T.N. and D.L.T. Anderson, 1994: Prospects for seasonal forecasting. *Q. J. Roy. Meteorol. Soc.*, **120**, 755-793.
- Pedlosky, J., 1979: Geophysical Fluid Dynamics. Springer-Verlag, pp710.
- Reynolds, R.W. and T.M. Smith, 1994: Improved global sea surface temperature analysis. *J. Climate*, **7**, 929-948.
- Simmons, A.J. and B.J. Hoskins, 1976: Baroclinic instability on the sphere: normal modes of the primitive and quasigeostrophic equations. *J. Atmos. Sci.*, **33**, 1454-1477.
- Syu, H.-H., J.D. Neelin and D.S. Gutzler, 1995: Seasonal and interannual variability in a hybrid coupled GCM. *J. Climate*, **9**, 2121-2143.
- Thompson, C.J., 1998: Initial conditions for optimal growth in a coupled ocean-atmosphere model of ENSO. *J. Atmos. Sci.*, **55**, 537-557.
- Vialard, J. and P. Delecluse, 1998a: An OGCM study for the TOGA decade. Part I: Role of salinity in the physics of the western Pacific fresh pool. *J. Phys. Oceanogr.*, **28**, 1071-1088.
- Vialard, J. and P. Delecluse, 1998b: An OGCM study for the TOGA decade. Part II: Barrier layer formation and variability. *J. Phys. Oceanogr.*, **28**, 1089-1106.
- Vialard, J., C. Menkes, J.-P. Boulanger, P. Delecluse, E. Guilyardi, and M.J. McPhaden, 2001: A model study of oceanic mechanisms affecting equatorial Pacific sea surface temperature during the 1997-98 El Nino. *J. Phys. Oceanogr.*, **31**, 1649-1675.
- Weaver, A. T., Vialard, J., Anderson, D. L. T. and Delecluse, P., 2001: Three- and four-dimensional variational assimilation with a general circulation model of the tropical Pacific Ocean. *ECMWF Technical Memo.*, In preparation.
- Webster, P.J., 1972: Reponse of the tropical atmosphere to local steady forcing. *Mon. Wea. Rev.*, **100**, 518-541.

Xue, Y., M.A. Cane, S.E. Zebiak and M.B. Blumenthal, 1994: On the prediction of ENSO: A study with a low order Markov model. *Tellus*, **46A**, 512-528.

Xue, Y., M.A. Cane and S.E. Zebiak, 1997a: Predictability of a coupled model of ENSO using singular vector analysis. Part I: Optimal growth in seasonal background and ENSO cycles. *Mon. Wea. Rev.*, **125**, 2043-2056.

Xue, Y., M.A. Cane and S.E. Zebiak, 1997b: Predictability of a coupled model of ENSO using singular vector analysis. Part II: Optimal growth and forecast skill. *Mon. Wea. Rev.*, **125**, 2057-2073.